

Shaping Maximally Localized Wannier Functions via Discrete Adiabatic Transport

Yuji Hamai^{1,*} and Katsunori Wakabayashi^{1,2,†}

¹*Department of Nanotechnology for Sustainable Energy, School of Science and Technology,
Kwansei Gakuin University, Gakuen-Uegahara 1, Sanda, 669-1330, Japan*

²*National Institute for Materials Science (NIMS), Namiki 1-1, Tsukuba 305-0044, Japan*

(Dated: 2026-05-15)

Maximally localized Wannier functions (MLWFs) are conventionally constructed by iteratively minimizing a spread functional over a high-dimensional gauge landscape. In this work, we present a non-variational constructive algorithm that unifies gauge smoothing and the eigenvalue problem of the projected position operator into a single deterministic framework. We demonstrate that discrete adiabatic transport across band degeneracies emerges naturally as an integral part of the solution procedure for the position eigenvectors. In this transport-aligned gauge, the Bloch overlaps exhibit an approximately linear phase dependence, allowing the Wannier centers to be extracted via deterministic fixed-point iterations and self-consistent updates rather than spread-functional minimization. Benchmark calculations for one- and two-dimensional systems yield spreads and orbital shapes in good agreement with standard minimization schemes. Furthermore, this analytical approach transparently isolates the physical origin of the $\mathcal{O}(L)$ mesh-dependent spread scaling (L being the boundary seam resolution) observed in graphene, demonstrating that it is an intrinsic geometric manifestation of non-commuting projected position operators forcing finite gauge defects to accumulate along a one-dimensional boundary seam.

I. INTRODUCTION

Wannier functions (WFs) provide an orthogonal, localized, and translationally invariant real-space framework for electronic states and have been systematically analyzed since the early days of solid-state physics [1–5]. A central theme in the historical development of Wannier theory has been the search for exponentially localized WFs (ELWFs) [6–9]. Motivated both by theoretical interest and practical needs for localized basis sets, these studies laid the foundation for the framework of maximally localized WFs (MLWFs), which has since become a standard tool across condensed matter, materials science, and photonics [10–14].

MLWFs enable the construction of tight-binding-like Hamiltonians and facilitate quantitative analyses of polarization [15–17], orbital magnetization [18], and related properties, chemical bonding [19, 20], and photonic confinement [21–23]. They also provide the foundation for developments in topological electronic and photonic devices [24–26]. In parallel, the Berry phase and Wilson-loop frameworks have clarified the gauge structure behind WFs and their connection to band topology [27–31].

The canonical approach to constructing MLWFs, established by Marzari and Vanderbilt (MV) [10, 11], involves the numerical minimization of a spread functional with respect to unitary gauge transformations. While MV analytically showed that the minimum spread condition corresponds to a maximally smooth Berry connection, perfectly flattening this gauge is only possible in one-dimensional systems. In two or higher dimensions, finding such a globally smooth gauge is fundamentally obstructed by the geometric frustration arising from the non-commutativity of the projected position operators, as explicitly formulated in the foundational works of MV

[10, 32]. Standard algorithms resolve this non-commutativity via an iterative spread minimization, which inherently acts as a variational global optimization that distributes this unavoidable geometric gauge mismatch across the entire Brillouin zone [10].

To make the gauge search more robust against the choice of initial conditions, significant advancements have been integrated into widely used open-source codes [13, 14]. These powerful refinements include optimized projections [33], density-matrix based localized orbitals (SCDM- k) [34, 35], and direct constructions via projected position operators in three dimensions [36].

In this paper, we propose a non-variational constructive algorithm by unifying gauge smoothing and the eigenvalue problem of the projected position operator (equivalently, the projected translation operator $e^{i\delta k \cdot \hat{x}}$) into a single deterministic framework. We demonstrate that discrete adiabatic transport, justified by Kato’s adiabatic theorem [37–40], naturally emerges as an integral part of the solution procedure for the position eigenvectors. Rather than performing a variational global optimization of a spread functional over the high-dimensional gauge manifold, this transport directly aligns the periodic parts of the Bloch functions across internal degeneracies to exhibit a linear phase dependence.

In this transport-aligned gauge, we derive a trigonometric equation for the Wannier centers, which is solved by a deterministic fixed-point iteration termed the “sinc-loop”. In the multiband case, the remaining numerical loops are fixed-point iterations and self-consistent updates for explicit center equations and projected-position matrices; they are not variational gauge searches over the spread functional. Crucially, because our sequential extraction approximately flattens the interior gauge along chosen one-dimensional strings instead of globally distributing the geometric mismatch, it transparently isolates the gauge frustration inherent in 2D systems. By applying our framework to graphene, we rigorously demonstrate that the anomalous $\mathcal{O}(L)$ mesh-dependent spread scal-

* hamai.sg@gmail.com

† ka.wakaba@gmail.com

ing (L being the boundary seam resolution) is not a numerical artifact, but an intrinsic geometric manifestation of non-commuting projected position operators forcing finite $\mathcal{O}(L^0)$ gauge defects to accumulate along a one-dimensional boundary seam.

The remainder of the paper is organized as follows: Section II defines the system and notations. Section III details the band peeling process via discrete adiabatic transport and its formal equivalence to the projected position operator framework. Sections IV and V introduce the constructive phase-alignment procedure and the sinc-loop iteration for multi-band systems. Section VI presents numerical benchmarks in 1D and 2D systems, culminating in the explicit reciprocal-space analysis of the boundary seam and the macroscopic spread divergence in graphene. Finally, Section VII summarizes our conclusions.

II. DESCRIPTION OF THE SYSTEM

This section introduces the notation and definitions used for 1D and 2D isolated composite-band systems.

A. Bloch Functions

The Bravais lattice of the system consists of L^d ($L \in \mathbb{Z}$) unit cells, $\Omega = [0, 1)^d$, which are labeled as follows:

$$\mathbb{M} = (\mathbb{Z}_L)^d, \quad (1)$$

where,

$$\mathbb{Z}_L = \left\{ M \in \mathbb{Z} : -\frac{L}{2} \leq M < \frac{L}{2} \right\}, \quad (2)$$

and it is assumed L is even. The set of lattice momenta of the system is given as follows:

$$\mathbb{K} = \left\{ \mathbf{k} = \delta k \mathbf{n} \mid \mathbf{n} \in (\mathbb{Z}_L)^d \right\}, \quad \delta k = \frac{2\pi}{L}. \quad (3)$$

The interior of the lattice momentum (open) space is also defined:

$$\mathbb{K}_I = \left\{ \mathbf{k} = \delta k \mathbf{n} \mid \mathbf{n} \in (\mathbb{Z}_I)^d \right\}, \quad (4)$$

where,

$$\mathbb{Z}_I = \left\{ M \in \mathbb{Z} : -\frac{L}{2} < M < \frac{L}{2} \right\}. \quad (5)$$

The Schrödinger equation of the system is:

$$\hat{H}|\psi_{\mathbf{k}}^n\rangle = \varepsilon_{\mathbf{k}}^n|\psi_{\mathbf{k}}^n\rangle, \mathbf{k} \in \mathbb{K}, n \in \mathbb{Z}_{>0}, \quad (6)$$

where \hat{H} is the Hamiltonian operator of the system and $\{|\psi_{\mathbf{k}}^n\rangle\}$ and $\{\varepsilon_{\mathbf{k}}^n\}$ are the eigenvectors and eigenvalues of the operator, respectively. The superscript n denotes the energy level or

band index of the eigenvector pertaining to the wave number \mathbf{k} . The eigenvectors, namely BFs, are further decomposed into the following form:

$$|\Psi_{\mathbf{k}}^n\rangle = L^{-d/2} e^{i\mathbf{k} \cdot \hat{\mathbf{x}}} |v_{\mathbf{k}}^n\rangle, \quad (7)$$

where $\{|v_{\mathbf{k}}^n\rangle\}$ is the set of cell-periodic solutions of the following Bloch Hamiltonian eigenvalue equation:

$$\hat{H}(\mathbf{k})|v_{\mathbf{k}}^n\rangle = \varepsilon_{\mathbf{k}}^n|v_{\mathbf{k}}^n\rangle, \quad (8)$$

where,

$$\hat{H}(\mathbf{k}) = e^{-i\mathbf{k} \cdot \hat{\mathbf{x}}} \hat{H} e^{i\mathbf{k} \cdot \hat{\mathbf{x}}}, \quad (9)$$

and $\{|v_{\mathbf{k}}^n\rangle\}$ are normalized as follows:

$$\langle v_{\mathbf{k}}^n | v_{\mathbf{k}}^n \rangle = \int_{\text{cell}} \bar{v}_{\mathbf{k}}^n(\mathbf{x}) v_{\mathbf{k}}^n(\mathbf{x}) d^d \mathbf{x} = 1. \quad (10)$$

The overline, e.g., $\bar{v}_{\mathbf{k}}^n$, denotes the complex conjugate of the respective variable. Since

$$\begin{aligned} \forall \mathbf{k}_1, \mathbf{k}_2 \in \mathbb{K}, \\ \text{Span}\{|v_{\mathbf{k}_1}^m\rangle \mid m \in \mathbb{Z}_{\geq 0}\} = \text{Span}\{|v_{\mathbf{k}_2}^m\rangle \mid m \in \mathbb{Z}_{\geq 0}\}, \end{aligned} \quad (11)$$

for all $|f\rangle$ satisfying:

$$\forall \mathbf{M} \in \mathbb{M}, \langle \mathbf{x} + \mathbf{M} | f \rangle = \langle \mathbf{x} | f \rangle, \quad (12)$$

the following holds:

$$\forall \mathbf{k} \in \mathbb{K}, |f\rangle = \sum_m |v_{\mathbf{k}}^m\rangle \langle v_{\mathbf{k}}^m | f \rangle. \quad (13)$$

B. State Space of Composite Energy Band System

Let the set of the energy bands $\{n_a, n_b, \dots, n_z\}$ composing the composite energy band under consideration be:

$$\mathbb{N}_C = \{n_a, n_b, \dots, n_z\}, \quad (14)$$

then the state space is spanned by the BFs described in Eq. (7):

$$\mathcal{H}_C = \text{Span}\{|\Psi_{\mathbf{k}}^n\rangle : \mathbf{k} \in \mathbb{K}, n \in \mathbb{N}_C\}, \quad (15)$$

To close the operation within \mathcal{H}_C , the following projection operator is introduced,

$$\hat{P}_{\mathcal{H}_C} = \sum_{n \in \mathbb{N}_C} \sum_{\mathbf{k} \in \mathbb{K}} |\Psi_{\mathbf{k}}^n\rangle \langle \Psi_{\mathbf{k}}^n|. \quad (16)$$

By using this, the following band projected operator is defined and it suppresses components protruding from \mathcal{H}_C , as well as filters out components outside \mathcal{H}_C as the input:

$$\tilde{A} = \hat{P}_{\mathcal{H}_C} \hat{A} \hat{P}_{\mathcal{H}_C}. \quad (17)$$

Another projection operator pertaining to the space spanned by the local frame at \mathbf{k} is defined as follows:

$$\hat{P}(\mathbf{k}) = \sum_{n \in \mathbb{N}_C} |v_{\mathbf{k}}^n\rangle \langle v_{\mathbf{k}}^n|. \quad (18)$$

C. Wannier Functions

The WFs are defined as follows:

$$\begin{aligned} |W_M^s\rangle &= L^{-d/2} \sum_{\mathbf{k}, n} e^{-i\mathbf{k} \cdot \mathbf{M}} f_{\mathbf{k}}^{s, n} |\psi_{\mathbf{k}}^n\rangle \\ &= L^{-d/2} \sum_{\mathbf{k}, n} e^{-i\mathbf{k} \cdot \mathbf{M}} e^{i\mathbf{k} \cdot \hat{\mathbf{x}}} f_{\mathbf{k}}^{s, n} |v_{\mathbf{k}}^n\rangle, \end{aligned} \quad (19)$$

with the condition:

$$\langle W_{M_1}^{s_1} | W_{M_2}^{s_2} \rangle = \delta_{M_1, M_2} \delta_{s_1, s_2}, \quad M_1, M_2 \in \mathbb{M}, \quad (20)$$

where M, M_1 and M_2 are the cell indices, and s indicates the series index in the composite band system and n denotes the band index. $f_{\mathbf{k}}^{s, n}$ is the (s, n) element of a unitary matrix transforming the periodic parts pertaining to band n to those pertaining to series, $\{|u_{\mathbf{k}}^s\rangle\}$:

$$|u_{\mathbf{k}}^s\rangle = \sum_n f_{\mathbf{k}}^{s, n} |v_{\mathbf{k}}^n\rangle, \quad (21)$$

and hence, the WF belonging to the series s is expressed:

$$|W_M^s\rangle = L^{-d/2} \sum_{\mathbf{k}} e^{-i\mathbf{k} \cdot \mathbf{M}} e^{i\mathbf{k} \cdot \hat{\mathbf{x}}} |u_{\mathbf{k}}^s\rangle. \quad (22)$$

From Eq. (20),

$$\begin{aligned} \mathcal{H}_C &= \text{Span}\{|\psi_{\mathbf{k}}^n\rangle : \mathbf{k} \in \mathbb{K}, n \in \mathbb{N}_C\} \\ &= \text{Span}\{|W_M^s\rangle : M \in \mathbb{M}, s \in \mathbb{N}_C\}. \end{aligned} \quad (23)$$

III. BAND PEELING FOR A COMPOSITE BAND WITH INTERNAL DEGENERACIES

We address an isolated composite-band subspace that may have internal degeneracies, while being separated from the rest of the spectrum by finite gaps throughout the Brillouin zone. We will also show that two ostensibly different viewpoints—(i) eigenvalue equation for $e^{i\delta\mathbf{k} \cdot \hat{\mathbf{x}}}$ and (ii) the multi-band adiabatic transport—coincide to first order in $|\delta\mathbf{k}|$, and provide a first-order accurate smoothing of gauge discontinuities in \mathbb{K}_J . We call this procedure band peeling to distinguish it from the variational disentanglement of Souza–Marzari–Vanderbilt [11], which selects an optimal subspace from energetically entangled bands.

Furthermore, it is shown that the adiabatic transport/projection in the current study is equivalent to Kato's parallel transport consistent with the gapless adiabatic framework of Avron and Elgart [37–39], which eventually provides a justification of the current procedures.

Throughout this section and the appendices, $|v_{\mathbf{k}}^n\rangle$ denotes the local energy-ordered periodic Bloch frame at each \mathbf{k} , indexed by the band label n , whereas $|u_{\mathbf{k}}^s\rangle$ denotes the peeled/transported frame indexed by the series label s .

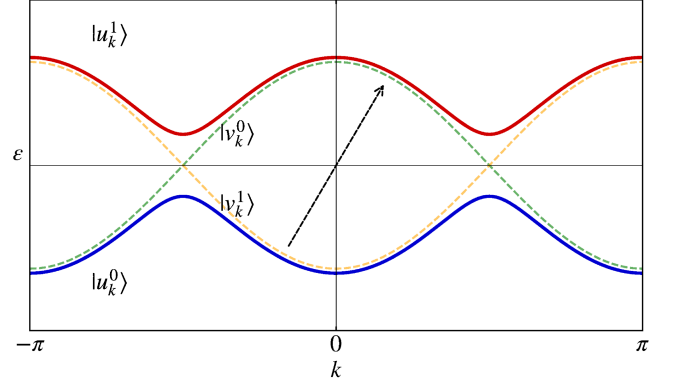


FIG. 1. (Color online) Schematic diagram of energy band peeling across degeneracy points. In the traditional band labeling, as shown with $|v_{\mathbf{k}}^n\rangle$, the bands are indexed locally in \mathbf{k} -space in ascending order from the bottom. On the other hand, the numbering indicated with $|u_{\mathbf{k}}^s\rangle$ provides a *smoother* connection. Mathematically, $|u_{\mathbf{k}}^s\rangle$ is projected to $\text{Span}\{|v_{\mathbf{k}+\delta\mathbf{k}}^m\rangle | m = 0, 1\}$ and becomes $|u_{\mathbf{k}+\delta\mathbf{k}}^s\rangle$.

A. Adiabatic change induced by $e^{i\delta\mathbf{k} \cdot \hat{\mathbf{x}}}$

As shown in Fig. 1, it is reasonable to assume that the *natural* connection of energy bands might be achieved by extending the energy bands with the adiabatic approximation [41, 42]. And hence, this section describes how the periodic parts of BFs are transformed by the adiabatic approximation.

Let $\hat{H}(\mathbf{k})$ be the *Hamiltonian* and $\varepsilon^n(t)$ be the instantaneous eigenvalue of the system,

$$\hat{H}(\mathbf{k})|v_{\mathbf{k}}^n\rangle = \varepsilon^n(t)|v_{\mathbf{k}}^n\rangle, \quad (24)$$

where \mathbf{k} is a function of time t :

$$\mathbf{k} = \mathbf{k}(t). \quad (25)$$

By expanding the transient solution $|\Psi(t)\rangle$ in the following way:

$$|\Psi(t)\rangle = \sum_n c_{\mathbf{k}}^n e^{-i\theta^n(t)} |v_{\mathbf{k}}^n\rangle, \quad (26)$$

and imposing the following equation:

$$i\hbar \frac{d}{dt} |\Psi(t)\rangle = \hat{H}(\mathbf{k}) |\Psi(t)\rangle, \quad (27)$$

we have (see Appendix A for details),

$$c_{\mathbf{k}+\delta\mathbf{k}}^m = \sum_n c_{\mathbf{k}}^n \langle v_{\mathbf{k}+\delta\mathbf{k}}^m | v_{\mathbf{k}}^n \rangle e^{i(\theta^m(t) - \theta^n(t))} + \mathcal{O}(\delta\mathbf{k}^2), \quad (28)$$

which leads to the following transport picture,

$$|\Psi(t + \delta t)\rangle = \left\{ \sum_m |v_{\mathbf{k}+\delta\mathbf{k}}^m\rangle \langle v_{\mathbf{k}+\delta\mathbf{k}}^m| \right\} \sum_n c_{\mathbf{k}}^n |v_{\mathbf{k}}^n\rangle e^{-i\theta^n(t)}, \quad (29)$$

with

$$\theta^n(t) = \frac{1}{\hbar} \int^t \varepsilon^n(\tau) d\tau. \quad (30)$$

When the initial condition is:

$$c_{\mathbf{k}}^n = \delta_{n,s}, \quad (31)$$

after setting the dynamical factor to unity, the state at \mathbf{k} develops to:

$$\begin{aligned} |u_{\mathbf{k}+\delta\mathbf{k}}^s\rangle &= |\Psi(\mathbf{k} + \delta\mathbf{k})\rangle \\ &= \left\{ \sum_m |v_{\mathbf{k}+\delta\mathbf{k}}^m\rangle \langle v_{\mathbf{k}+\delta\mathbf{k}}^m| \right\} |u_{\mathbf{k}}^s\rangle + \mathcal{O}(\delta\mathbf{k}^2). \end{aligned} \quad (32)$$

Since the projection is summation over all bands in the composite-band system and $|u_{\mathbf{k}}^s\rangle$ is projected to the closest vector at $\mathbf{k} + \delta\mathbf{k}$, the new indexing at $\mathbf{k} + \delta\mathbf{k}$ no longer depends on a particular local labeling of the energy bands denoted by m in Eq. (32), as shown in Fig. 1. Therefore, it eliminates at least the phase jump coming from band indexing.

B. Eigenvalue Equation for $e^{i\delta\mathbf{k}\cdot\hat{\mathbf{x}}}$

This subsection derives the solution procedure of the eigenvalue problem of the translation operator, $e^{i\delta\mathbf{k}\cdot\hat{\mathbf{x}}}$. For this operator the following equations hold:

$$\begin{aligned} \langle \Psi_{\mathbf{k}}^m | e^{i\delta\mathbf{k}\cdot\hat{\mathbf{x}}} | W_0^s \rangle &= \sum_n \int_{\mathbf{k}-\delta\mathbf{k}}^{s,n} \langle v_{\mathbf{k}}^m | v_{\mathbf{k}-\delta\mathbf{k}}^n \rangle + \mathcal{O}(\delta\mathbf{k}^2) \\ \langle \Psi_{\mathbf{k}}^m | e^{i\delta\mathbf{k}\cdot\hat{\mathbf{x}}} | W_0^s \rangle &= e^{i\delta\mathbf{k}\cdot\mathbf{x}_0} f_{\mathbf{k}}^{s,m}, \end{aligned} \quad (33)$$

and hence, it leads to the following equation composed of the periodic parts (see Appendix B for details):

$$f_{\mathbf{k}}^{s,m} = e^{-i\delta\mathbf{k}\cdot\mathbf{x}_0} \sum_n \int_{\mathbf{k}-\delta\mathbf{k}}^{s,n} \langle v_{\mathbf{k}}^m | v_{\mathbf{k}-\delta\mathbf{k}}^n \rangle + \mathcal{O}(\delta\mathbf{k}^2), \quad (34)$$

By multiplying $|v_{\mathbf{k}}^n\rangle$ to both sides and summing over n , the energy bands are reconstructed and the following projection equation yields:

$$|u_{\mathbf{k}}^s\rangle = e^{-i\delta\mathbf{k}\cdot\mathbf{x}_0} \left\{ \sum_m |v_{\mathbf{k}}^m\rangle \langle v_{\mathbf{k}}^m| \right\} |u_{\mathbf{k}-\delta\mathbf{k}}^s\rangle + \mathcal{O}(\delta\mathbf{k}^2), \quad (35)$$

The *twist* $e^{-i\delta\mathbf{k}\cdot\mathbf{x}_0}$ [43] has to be determined separately, so that it reconciles the phase jumps across the border of the \mathbf{k} -space after summation over the \mathbf{k} -space as seen in Eq. (33). Before proceeding, we note explicitly that Eq. (35) reduces to Eq. (32) once the twist is removed, $\mathbf{x}_0 = \mathbf{0}$, and the wave

number is shifted as $\mathbf{k} \rightarrow \mathbf{k} + \delta\mathbf{k}$:

$$\text{Eq. (35)} \xrightarrow[\mathbf{x}_0=\mathbf{0}]{\mathbf{k}\rightarrow\mathbf{k}+\delta\mathbf{k}} |u_{\mathbf{k}+\delta\mathbf{k}}^s\rangle = \left\{ \sum_m |v_{\mathbf{k}+\delta\mathbf{k}}^m\rangle \langle v_{\mathbf{k}+\delta\mathbf{k}}^m| \right\} |u_{\mathbf{k}}^s\rangle + \mathcal{O}(|\delta\mathbf{k}|^2),$$

which is precisely Eq. (32).

C. Underlying Symmetry of the Adiabatic Expansion

The primary objective of this subsection is to explicitly demonstrate that the discrete adiabatic transport (Eq. (32)) and the eigenvalue equation of the projected translation operator (Eq. (35)) are formally equivalent and originate from the same first-order geometric transport.

Dropping the explicit time dependence of Eq. (29) is equivalent to setting the left-hand side of Eq. (27) to zero. Equivalently, for any orthonormal frame $\{|v_{\mathbf{k}}^m\rangle\}$, at \mathbf{k} ,

$$\left\{ \sum_m |v_{\mathbf{k}}^m\rangle \langle v_{\mathbf{k}}^m| \right\} \frac{d}{dt} |\Psi(\mathbf{k}(t))\rangle = 0, \quad (36)$$

where the summation is performed over all relevant band indices. Since $|\Psi(\mathbf{k})\rangle$ depends on t only through $\mathbf{k}(t)$, the following equation then holds:

$$\delta t \left\{ \sum_m |v_{\mathbf{k}}^m\rangle \langle v_{\mathbf{k}}^m| \right\} \frac{d\mathbf{k}}{dt} \cdot \nabla_{\mathbf{k}} |\Psi(\mathbf{k}(t))\rangle = 0, \quad (37)$$

where δt is an infinitesimally short time duration. If $\{|u_{\mathbf{k}}^s\rangle\}$ is a specific realization of $|\Psi(\mathbf{k})\rangle$, by replacing $\delta t (d\mathbf{k}/dt)$ with $\delta\mathbf{k}$, the following equation has to hold:

$$\begin{aligned} \left\{ \sum_m |v_{\mathbf{k}}^m\rangle \langle v_{\mathbf{k}}^m| \right\} \delta\mathbf{k} \cdot \nabla_{\mathbf{k}} |u_{\mathbf{k}}^s\rangle &= \left\{ \sum_m |v_{\mathbf{k}}^m\rangle \langle v_{\mathbf{k}}^m| \right\} \{ |u_{\mathbf{k}}^s\rangle - |u_{\mathbf{k}-\delta\mathbf{k}}^s\rangle \} \\ &= 0. \end{aligned} \quad (38)$$

Thus we arrive at Eq. (35) without the twist.

$$|u_{\mathbf{k}}^s\rangle = \left\{ \sum_m |v_{\mathbf{k}}^m\rangle \langle v_{\mathbf{k}}^m| \right\} |u_{\mathbf{k}-\delta\mathbf{k}}^s\rangle. \quad (39)$$

Therefore, the role of the adiabatic expansion/transport in the present construction is to make the transported local subspace spanned by $\{|u_{\mathbf{k}}^s\rangle\}$ as uniform as possible along the transport direction. In this sense, the transport virtually removes one degree of gauge discontinuity from the Bloch frame by enforcing first-order consistency between neighboring local subspaces.

Although the adiabatic expansion is introduced from the Schrödinger equation with the Bloch Hamiltonian $\hat{H}(\mathbf{k})$, the Hamiltonian plays no direct role in the construction from Eq. (36) onward. Its role in the peeling and in identifying the eigenvectors of the projected position/translation operator is only to specify the family of composite-band subspaces at each \mathbf{k} . The essential content of the adiabatic transport, as expressed in Eq. (36), is that the periodic part should remain unchanged to first order along the transport direction $d\mathbf{k}/dt$,

and hence along $\delta\mathbf{k}$.

D. Kato's transport and justification of the adiabatic transport in the presence of internal degeneracies

In standard treatments of the adiabatic theorem, one typically assumes that the instantaneous eigenstates are nondegenerate. Here we justify the use of Eq. (32) for isolated composite-band systems in the presence of internal degeneracy.

In the works of Kato, Avron and Elgart [37–39], the validity of the adiabatic theorem is investigated, and they have shown that the approximation is valid even when gaps close, as long as,

$$\hat{P}(\mathbf{k}) = \sum_{m \in \mathbb{N}_C} |v_{\mathbf{k}}^m\rangle \langle v_{\mathbf{k}}^m| \in C^1. \quad (40)$$

In their formula, the state at \mathbf{k} evolves in the following way,

$$|\Psi_{\mathbf{k}+\delta\mathbf{k}}\rangle = \hat{U}(\mathbf{k})|\Psi_{\mathbf{k}}\rangle, \quad (41)$$

where,

$$\begin{aligned} \dot{\hat{U}}(\mathbf{k}) &= -i\hat{E}(\mathbf{k})\hat{U}(\mathbf{k}) \\ \hat{E}(\mathbf{k}) &= i \left[\dot{\hat{P}}(\mathbf{k}), \hat{P}(\mathbf{k}) \right], \end{aligned} \quad (42)$$

and \mathbf{k} is a function of t and the dot, e.g., $\dot{P}(\mathbf{k})$, denotes the time derivative of the respective variable. The first order solution is thus, given as follows:

$$\hat{U}(\mathbf{k}) = I - i\delta t \hat{E}(\mathbf{k}) + \mathcal{O}(\delta k^2), \quad (43)$$

By limiting the initial states at \mathbf{k} and final states at $\mathbf{k} + \delta\mathbf{k}$ in the composite energy bands (see Appendix C 1 for details),

$$\begin{aligned} \hat{P}(\mathbf{k} + \delta\mathbf{k})\hat{U}(\mathbf{k})\hat{P}(\mathbf{k}) &= \hat{P}(\mathbf{k} + \delta\mathbf{k})\hat{P}(\mathbf{k}) + (\delta\mathbf{k}\nabla\hat{P}(\mathbf{k}))^2\hat{P}(\mathbf{k}) \\ &= \hat{P}(\mathbf{k} + \delta\mathbf{k})\hat{P}(\mathbf{k}) + \mathcal{O}(|\delta\mathbf{k}|^2). \end{aligned} \quad (44)$$

And hence, the following propagation/translation equation is obtained,

$$\begin{aligned} |u_{\mathbf{k}+\delta\mathbf{k}}^s\rangle &= \hat{P}(\mathbf{k} + \delta\mathbf{k})\hat{U}(\mathbf{k})\hat{P}(\mathbf{k})|u_{\mathbf{k}}^s\rangle \\ &= \hat{P}(\mathbf{k} + \delta\mathbf{k})\hat{P}(\mathbf{k})|u_{\mathbf{k}}^s\rangle \\ &= \left\{ \sum_{m_1} |v_{\mathbf{k}+\delta\mathbf{k}}^{m_1}\rangle \langle v_{\mathbf{k}+\delta\mathbf{k}}^{m_1}| \right\} \left\{ \sum_{m_2} |v_{\mathbf{k}}^{m_2}\rangle \langle v_{\mathbf{k}}^{m_2}| \right\} |u_{\mathbf{k}}^s\rangle \\ &= \sum_m |v_{\mathbf{k}+\delta\mathbf{k}}^m\rangle \langle v_{\mathbf{k}+\delta\mathbf{k}}^m| u_{\mathbf{k}}^s, \end{aligned} \quad (45)$$

which coincides with the geometrical parts of Eq. (32). Therefore, Eq. (32) is justified at first order for isolated composite-band systems even in the presence of internal degeneracies, without assuming a uniform spectral gap, provided $\hat{P}(\mathbf{k})$ remains C^1 along the path.

E. Correction to Eqs. (32) and (35) based on Kato's formula

There are two practical differences between Kato's transport and the first-order projection described by Eqs. (32) and (35). First, the latter employ a one-sided finite-difference step; this is not essential and can be improved by higher-order schemes. Second, the overlap matrix between the frames at \mathbf{k} and $\mathbf{k} + \delta\mathbf{k}$ is not exactly unitary at finite mesh spacing. We enforce unitarity by replacing it with the unitary factor of the polar decomposition via singular value decomposition (SVD) [43].

Writing the projected vectors as,

$$|u_{\mathbf{k}+\delta\mathbf{k}}^s\rangle = \sum_{m \in \mathbb{N}_C} |v_{\mathbf{k}+\delta\mathbf{k}}^m\rangle \langle v_{\mathbf{k}+\delta\mathbf{k}}^m| u_{\mathbf{k}}^s\rangle = \sum_m M_{m,s} |v_{\mathbf{k}+\delta\mathbf{k}}^m\rangle, \quad (46)$$

where,

$$M_{m,s} = \langle v_{\mathbf{k}+\delta\mathbf{k}}^m| u_{\mathbf{k}}^s\rangle, \quad (47)$$

we compute the SVD $M = V\Sigma W^\dagger$ with $\Sigma = \text{diag}(\sigma_1, \dots, \sigma_J)$ and define the unitary polar factor,

$$Q = VW^\dagger. \quad (48)$$

The orthonormalized transport step is then,

$$|u_{\mathbf{k}+\delta\mathbf{k}}^s\rangle = \sum_m |v_{\mathbf{k}+\delta\mathbf{k}}^m\rangle Q_{m,s}. \quad (49)$$

IV. FIXING WANNIER CENTER AND INITIAL CONDITION OF $|u_{\mathbf{k}}^s\rangle$

Since the parallel transport Eqs. (32) and (35) alone do not provide the initial condition of $\{f_{\mathbf{k}}^{s,n}\}$ nor fix the Wannier center \mathbf{x}_0 , this section is devoted to solving these problems. It should be noted, however, that when the following condition,

$$\langle u_{\mathbf{k}}^{s_0}| u_{\mathbf{k}}^{s_1}\rangle = \delta_{s_0,s_1}, \quad (50)$$

is satisfied, the periodic parts remain approximately orthogonal, as detailed in Appendix C 2,

$$\langle u_{\mathbf{k}+\delta\mathbf{k}}^{s_0}| u_{\mathbf{k}+\delta\mathbf{k}}^{s_1}\rangle = \delta_{s_0,s_1} + \mathcal{O}(\delta k^2). \quad (51)$$

And hence, by provisionally setting,

$$|u_{\mathbf{k}_0}^s\rangle = |v_{\mathbf{k}_0}^s\rangle, \quad (52)$$

somewhere in the \mathbf{k} -space, where the energy bands are reasonably separated, the obtained WFs are approximately orthogonal up to the first order of $\delta\mathbf{k}$ and resemble the right eigenvectors of the projected translation operator except the Wannier center and the initial value of $\{f_{\mathbf{k}_0}^{s,n}\}$.

A. Fixing the Initial Condition of $\{f_{\mathbf{k}}^{s,n}\}$

By using the provisional WFs $\{|w_0^s\rangle\}$, the right MLWFs, $\{|W_0^s\rangle\}$, the eigenvectors of a position operator, have to be obtained by applying a unitary transformation,

$$|W_0\rangle = |w_0\rangle F, \quad (53)$$

if expressed element-by-element:

$$\begin{bmatrix} |W_0^0\rangle & |W_1^0\rangle & \dots & |W_{N_C-1}^0\rangle \end{bmatrix} = \begin{bmatrix} |w_0^0\rangle & |w_0^1\rangle & \dots & |w_0^{N_C-1}\rangle \end{bmatrix} \begin{bmatrix} F_0^0 & F_0^1 & \dots & F_0^{N_C-1} \\ F_1^0 & F_1^1 & \dots & F_1^{N_C-1} \\ \vdots & \vdots & \ddots & \vdots \\ F_{N_C-1}^0 & F_{N_C-1}^1 & \dots & F_{N_C-1}^{N_C-1} \end{bmatrix}. \quad (54)$$

By requiring $|W_0\rangle$ to be the eigenvectors of the position operator \hat{x} , we have the following eigenvalue equation.

$$\begin{aligned} \langle W_0|\hat{x}|W_0\rangle &= F^\dagger \langle w_0|\hat{x}|w_0\rangle F \\ &= F^\dagger X F \\ &= \Lambda, \end{aligned} \quad (55)$$

where, X is the matrix representation of \hat{x} calculated with the provisional WFs, $\{|w_0^s\rangle\}$, and Λ is the diagonal eigenvalue matrix. F , the eigenvector matrix of the eigenvalue equation, is easily obtained with a numerical library, such as the GNU Scientific Library (GSL) [44]. And hence, the arbitrariness of the initial condition of $\{f_{\mathbf{k}}^{s,n}\}$ is fixed and the Wannier centers are obtained from Λ .

In the current study, $\{f_{\mathbf{k}}^{s,n}\}$ is provisionally fixed at \mathbf{k} where all energy bands in the composite system are separated with reasonable sizes of energy gaps, e.g., $\mathbf{k}_0 = (\pi, \pi)$ in the case of lower energy bands of graphene,

$$f_{\mathbf{k}_0}^{s,n} = \delta_{s,n}. \quad (56)$$

Accordingly, the initial condition is revised as follows:

$$f_{\mathbf{k}_0}^{s,n} = \sum_p \delta_{p,n} F_{s,p}. \quad (57)$$

B. Fixing Wannier Centers

By solving Eq. (55), the Wannier centers are, theoretically, obtained as the elements of the diagonal eigenvalue matrix Λ . In a numerical context, the values of $X = \langle w_0|\hat{x}|w_0\rangle$ are affected by the concentration of $w(x) = \langle x|w_0\rangle$, which recursively depends on the Wannier centers given in Λ . Thus, an iterative method to obtain the Wannier centers with theoretically guaranteed stability is introduced. In practice, the coupled determination of X and Λ implied by Eq. (55) is handled iteratively; this is a numerical solver for the explicit equations, not a search or minimization over a spread functional.

In this subsection, the WFs are treated series by series through Eq. (55), and hence the superscript indicating its se-

ries is dropped.

1. Wannier Group and Transformation

From the periodic parts $\{|u_{\mathbf{k}}\rangle\}$, obtained from Eqs. (33), (55) and (57), we have a WF with a candidate Wannier center \mathbf{r} ,

$$|W_M(\mathbf{r})\rangle = L^{-d/2} \sum_{\mathbf{k}} e^{-i\mathbf{r}\cdot\mathbf{k}} e^{i\mathbf{k}\cdot(\hat{\mathbf{x}}-M)} |u_{\mathbf{k}}\rangle, \quad \mathbf{r} \in [0, 1)^d. \quad (58)$$

We further define sets labeled by \mathbf{r} ,

$$\mathcal{G}_{\mathbf{r}}^s = \{|W_M(\mathbf{r})\rangle : M \in \mathbb{M}\}. \quad (59)$$

Since the space spanned by the elements of each group has to be identical,

$$\text{Span}\{\mathcal{G}_p\} = \text{Span}\{\mathcal{G}_r\} \quad \forall \mathbf{r}, \mathbf{p} \in [0, 1)^d. \quad (60)$$

A transformation between them must exist, and it is given by:

$$|W_M(\mathbf{r})\rangle = \sum_N \prod_{\mu=1}^d \text{sinc}(M_\mu - N_\mu + r_\mu - p_\mu) |W_N(\mathbf{p})\rangle, \quad (61)$$

where,

$$\text{sinc}x = \frac{\sin \pi x}{\pi x}, \quad (62)$$

and the following approximation is utilized (see Appendix D 1 for details and simplified calculations),

$$\frac{1}{L} \lim_{\delta k \rightarrow 0} \sum_{\mathbf{k}} e^{-i\mathbf{k}(M-N+r-p)} = \text{sinc}(M-N+r-p). \quad (63)$$

Matrix elements calculated by basis belonging to different groups are also transformed in the following way,

$$\begin{aligned} X_{M_1 M_2}(r) &= \langle W_{M_1}(\mathbf{r})|\hat{x}|W_{M_2}(\mathbf{r})\rangle \\ &= \sum_{N_1, N_2} \prod_{\mu=1}^d \text{sinc}(M_{1,\mu} - N_{1,\mu} + r_\mu - p_\mu) \cdot \\ &\quad \prod_{\mu=1}^d \text{sinc}(M_{2,\mu} - N_{2,\mu} + r_\mu - p_\mu) X_{N_1 N_2}(\mathbf{p}). \end{aligned} \quad (64)$$

2. Finding Wannier center of MLWFs

For the sake of conciseness and clarity, the derivation of the method to obtain Wannier centers is done in a 1D model. The multidimensional formulation is given in Appendix D 4.

A WF in 1D with a fractional shift r is given as follows:

$$|W_M(r)\rangle = \frac{1}{\sqrt{L}} \sum_{\mathbf{k}} e^{-ikr} e^{ik(\hat{x}-M)} |u_{\mathbf{k}}\rangle. \quad (65)$$

Let us assume that the right value $r = x_0$ is found, then the following holds:

$$\langle W_M(x_0)|\hat{x}|W_N(x_0)\rangle = \delta_{M,N}(M+x_0). \quad (66)$$

Equation (64) relates the above to a known, calculable value,

$$X_{0,0}(r) = \langle W_0(r)|\hat{x}|W_0(r)\rangle, \quad (67)$$

and using Eq. (D5), we have:

$$\begin{aligned} X_{0,0}(r) &= \sum_{M,N} \text{sinc}(M+x_0-r) \text{sinc}(N+x_0-r) \delta_{M,N}(M+x_0) \\ &= \frac{\sin 2\pi(x_0-r)}{2\pi} + r. \end{aligned} \quad (68)$$

$X_{0,0}^r$ is implicitly related to x_0 via the right-hand side of Eq. (67). And hence, the following two iterative dynamics are identical,

$$r^{n+1} = \langle W_0(r^n)|\hat{x}|W_0(r^n)\rangle, \quad (69)$$

$$r^{n+1} = \frac{\sin(2\pi(x_0-r^n))}{2\pi} + r^n, \quad (70)$$

where n appearing on the shoulder of r is the iteration number. The former (Eq. (69)) is used for the actual numerical calculation, while the latter (Eq. (70)) reveals the underlying mathematical structure and is used to prove convergence. Through the iteration described in Eqs. (69) and (70), the following holds, as detailed in Appendix D 2.

$$\lim_{n \rightarrow \infty} r^n = x_0. \quad (71)$$

This fixed-point dynamics is illustrated by the cobweb diagram in Fig. 2.

Note that Eq. (73) itself is a solvable equation with given $X_{0,0}(r)$ with no iteration. The numerically obtained $X_{0,0}(r)$, in reality, contains errors coming from the specific settings. Applying the iteration, therefore, appears to be a better choice. Even in multi-dimensional cases, by letting,

$$X_{M_1, M_2}(x_0) = \delta_{M_1, x, M_2, x} \delta_{M_1, y, M_2, y} \delta_{M_1, z, M_2, z} (M_{1, x} + x_0), \quad (72)$$

the following similarly holds, as described in Appendix D 4,

$$X_{00}(r) = \frac{\sin 2\pi(x_0-r_x)}{2\pi} + r_x, \quad (73)$$

and hence the above argument also applies.

Alternatively, rather classical derivation and the numerical verification are found in Appendix D 3.

For later numerical sections, the overall constructive numerical workflow is summarized in Fig. 3. The iterative part of this workflow should be understood as a solver comprising fixed-point iterations and self-consistent updates for center parameters and projected-position matrices, not as a variational

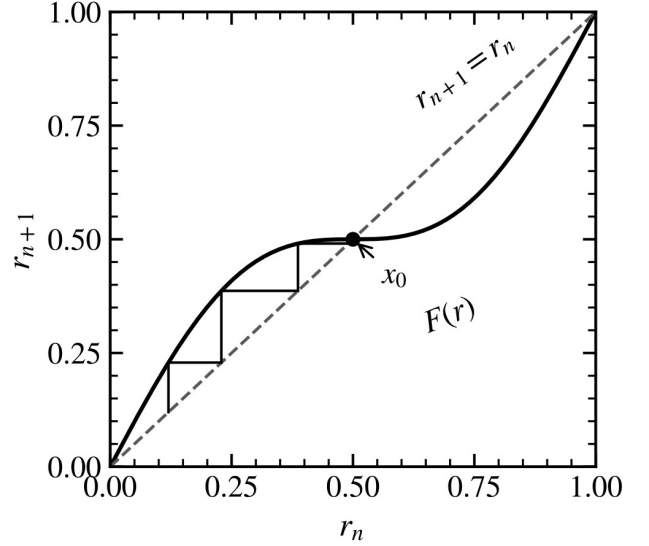


FIG. 2. Cobweb diagram for the fixed-point iteration $r^{n+1} = r^n + \sin[2\pi(x_0 - r^n)]/(2\pi) \pmod{1}$. The dashed line denotes $r^{n+1} = r^n$. For any start $r_0 \neq x_0 \pm \frac{1}{2} \pmod{1}$, the iteration converges to x_0 with a cubic (third-order) local rate.

spread minimization.

V. SINGLE-BAND SYSTEM

Before moving to benchmarks, we specialize the general framework to an isolated single band, where the gauge group reduces to $U(1)$. In this limit, it is easier to see how the phase flattening done by the transport actually contributes to minimizing the spread, since the spread functional is reduced to an analytic Euler–Lagrange equation, a k-space Poisson problem.

In a single band system, $f_k^{s,n}$ is reduced to:

$$f_k^{s,n} \rightarrow e^{i\phi_k}, \phi_k \in \mathbb{R}, \quad (74)$$

and hence, the BFs and WFs are expressed as follows:

$$\begin{cases} |\psi_k\rangle = L^{-d/2} e^{ik \cdot \hat{x}} |v_k\rangle \\ |W_M\rangle = \frac{1}{\sqrt{L}} \sum_k e^{-ik \cdot M} e^{ik \cdot \hat{x}} |u_k\rangle \\ |u_k\rangle = e^{i\phi_k} |v_k\rangle. \end{cases} \quad (75)$$

A. Berry Connection

By introducing $\theta_k(x)$, the phase of $v_k(x)$, as follows:

$$v_k(x) = |v_k(x)| e^{i\theta_k(x)} \quad (\theta_k(x) \in \mathbb{R}), \quad (76)$$

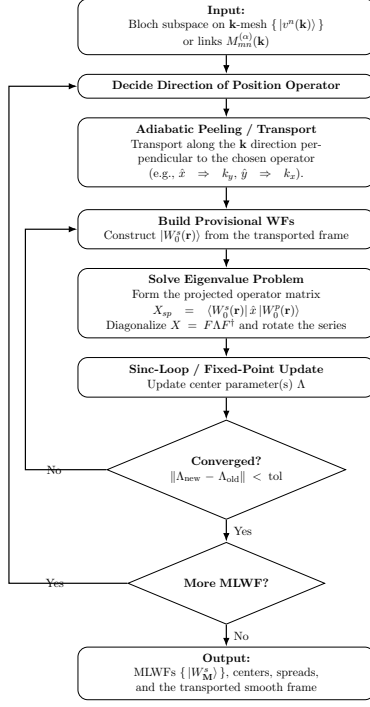


FIG. 3. Flowchart of the constructive numerical workflow used in the later results sections. The algorithm combines adiabatic peeling with fixed-point iterations and self-consistent updates of the Wannier centers and projected-position matrices, followed by sequential extraction of localized orbitals.

the Berry connection $\langle v_k | v_{k-\delta k} \rangle$ for $-\pi < k < \pi$ is calculated as follows:

$$\begin{aligned} \langle v_k | v_{k-\delta k} \rangle &= \langle v_k | v_k \rangle - \delta k \langle v_k | \nabla_k | v_k \rangle + \mathcal{O}(\delta k^2) \\ &= 1 - i \delta k \cdot \mathbf{A}_k + \mathcal{O}(\delta k^2), \end{aligned} \quad (77)$$

where,

$$\mathbf{A}_k = -i \langle v_k | \nabla_k | v_k \rangle. \quad (78)$$

By utilizing,

$$\nabla_k \int d^d x |v_k(x)|^2 = 0, \quad (79)$$

\mathbf{A}_k is also expressed as follows:

$$\mathbf{A}_k = \int d^d x |v_k(x)|^2 \nabla_k \theta_k(x). \quad (80)$$

Note that \mathbf{A}_k is decomposed into the transverse and longitudinal part:

$$\mathbf{A}_k = \mathbf{A}_k^T + \nabla_k \varphi_k, \quad \nabla_k \cdot \mathbf{A}_k^T = 0. \quad (81)$$

B. Minimum Spread Condition

To find out a constraint on ϕ_k^n in \mathbb{K}_J , the functional equation for the minimum spread is reviewed. The spread of a WF with its center at \mathbf{x}_0 is calculated as follows [10]:

$$\begin{aligned} \sigma(\mathbf{x}^2) &= \langle W_0 | (\hat{\mathbf{x}} - \mathbf{x}_0)^2 | W_0 \rangle \\ &= \langle W_0 | \hat{\mathbf{x}}^2 | W_0 \rangle - \mathbf{x}_0^2, \end{aligned} \quad (82)$$

where \mathbf{x}_0 is the Wannier center. The minimum spread is therefore achieved, when the following is minimized:

$$\begin{aligned} \langle \hat{\mathbf{x}}^2 \rangle &= \langle W_0 | \hat{\mathbf{x}}^2 | W_0 \rangle \\ &= \frac{1}{L^d} \sum_{\mathbf{k}} \langle \nabla_{\mathbf{k}} u_{\mathbf{k}} | \nabla_{\mathbf{k}} u_{\mathbf{k}} \rangle \\ &= \frac{1}{L^d} \sum_{\mathbf{k}} \int d^d x (\nabla_{\mathbf{k}} |v_{\mathbf{k}}(\mathbf{x})|)^2 + |v_{\mathbf{k}}(\mathbf{x})|^2 \{ \nabla_{\mathbf{k}} (\theta_{\mathbf{k}} + \phi_{\mathbf{k}}) \}^2. \end{aligned} \quad (83)$$

By utilizing Eq. (80) and approximating the summation with integration, the functional derivative of Eq. (83) is given as follows [45–48],

$$\begin{aligned} \left\langle \frac{\delta \hat{\mathbf{x}}^2[\phi]}{\delta \phi}, \lambda \right\rangle &= \frac{1}{\pi^d} \frac{d}{d\varepsilon} \int d^d k \int d^d x |v_{\mathbf{k}}(\mathbf{x})|^2 \cdot \\ &\quad \left. |\nabla_{\mathbf{k}} (\theta_{\mathbf{k}}(\mathbf{x}) + \phi_{\mathbf{k}} + \varepsilon \lambda_{\mathbf{k}})|^2 \right|_{\varepsilon=0} \quad (84) \\ &= \frac{2}{\pi^d} \int d^d k (\mathbf{A}_{\mathbf{k}} + \nabla_{\mathbf{k}} \phi_{\mathbf{k}}) \cdot \nabla_{\mathbf{k}} \lambda_{\mathbf{k}} \\ &= -\frac{2}{\pi^d} \int d^d k \lambda_{\mathbf{k}} (\nabla_{\mathbf{k}} \cdot \mathbf{A}_{\mathbf{k}} + \Delta_{\mathbf{k}} \phi_{\mathbf{k}}), \end{aligned}$$

where $\Delta_{\mathbf{k}}$ is the Laplacian operator in the \mathbf{k} -space, and $\lambda_{\mathbf{k}}$ is an arbitrary trial function satisfying the following (see Eq. (3)):

$$\lambda_{\mathbf{k}}|_{\partial \mathbb{K}} = 0. \quad (85)$$

Thus, the minimum spread condition is expressed in the following partial differential equation (see Eq. (4)),

$$\Delta_{\mathbf{k}} \phi_{\mathbf{k}} + \nabla_{\mathbf{k}} \cdot \mathbf{A}_{\mathbf{k}} = 0, \quad \mathbf{k} \in \mathbb{K}_J, \quad (86)$$

Denoting a particular solution by $\phi_{\mathbf{k}}^0$, we have a family of solutions,

$$\phi_{\mathbf{k}} = \phi_{\mathbf{k}}^0 + \mathbf{k} \cdot \mathbf{x}_0, \quad (87)$$

where $\mathbf{k} \cdot \mathbf{x}_0$ represents a homogeneous solution. Hence, the Berry connection made of $\{|u_{\mathbf{k}}\rangle\}$ is,

$$\tilde{\mathbf{A}}_{\mathbf{k}} = \mathbf{A}_{\mathbf{k}} + \nabla_{\mathbf{k}} \phi_{\mathbf{k}}. \quad (88)$$

Thus,

$$\nabla_{\mathbf{k}} \cdot \tilde{\mathbf{A}}_{\mathbf{k}} = 0. \quad (89)$$

If the band admits an ELWF and an MLWF, and if, in addition,

$$\mathbf{A}_{\mathbf{k}}^T = 0, \quad (90)$$

then Eqs. (86) and (89) have a solution of the form,

$$\tilde{\mathbf{A}}_{\mathbf{k}} = -\mathbf{x}_0. \quad (91)$$

From the above,

$$\begin{aligned} \langle u_{\mathbf{k}} | u_{\mathbf{k}+\delta\mathbf{k}} \rangle &= \langle u_{\mathbf{k}} | \{ |u_{\mathbf{k}}\rangle + \delta\mathbf{k} \cdot \nabla_{\mathbf{k}} |u_{\mathbf{k}}\rangle \} + \mathcal{O}(\delta\mathbf{k}^2) \\ &= \langle u_{\mathbf{k}} | u_{\mathbf{k}} \rangle + i\delta\mathbf{k} \cdot \tilde{\mathbf{A}}_{\mathbf{k}} + \mathcal{O}(\delta\mathbf{k}^2) \\ &= 1 - i\delta\mathbf{k} \cdot \mathbf{x}_0 + \mathcal{O}(\delta\mathbf{k}^2). \end{aligned} \quad (92)$$

The last line is the infinitesimal form of a phase-plane relation. Indeed, to first order in the mesh spacing,

$$1 - i\delta\mathbf{k} \cdot \mathbf{x}_0 = e^{-i\delta\mathbf{k} \cdot \mathbf{x}_0} + \mathcal{O}(\delta\mathbf{k}^2). \quad (93)$$

Equivalently, if $\mathbf{k}(t)$ is a path in \mathbb{K}_J and

$$\theta(t) = \arg\langle u_{\mathbf{k}(0)} | u_{\mathbf{k}(t)} \rangle,$$

then Eq. (92) gives the first-order phase equation

$$\frac{d\theta}{dt} = -\dot{\mathbf{k}}(t) \cdot \mathbf{x}_0. \quad (94)$$

Integrating this relation along a link from \mathbf{k}_1 to \mathbf{k}_2 gives the finite-link phase factor. For a finite link, the numerical overlap may also have a positive modulus. Since the present discussion concerns the phase-plane relation, this positive modulus is understood to be separated off, and only the unit-modulus phase factor is written explicitly below. In vector form and in the two-dimensional component form used below, this phase factor is

$$\begin{aligned} e^{i\arg\langle u_{\mathbf{k}_1} | u_{\mathbf{k}_2} \rangle} &= e^{-i(\mathbf{k}_2 - \mathbf{k}_1) \cdot \mathbf{x}_0} \\ &= e^{i(k_{1x} - k_{2x})x_0} e^{i(k_{1y} - k_{2y})y_0}, \end{aligned} \quad (95)$$

where $\mathbf{k}_1, \mathbf{k}_2 \in \mathbb{K}_J$. The first line follows from the constant-connection condition Eq. (91), while the second line is the two-dimensional component form of the same phase factor.

Equivalently, Eq. (95) gives the following phase-plane equation:

$$\begin{aligned} \arg\langle u_{\mathbf{k}_1} | u_{\mathbf{k}_2} \rangle &= (\mathbf{k}_1 - \mathbf{k}_2) \cdot \mathbf{x}_0 \\ &= (k_{1x} - k_{2x})x_0 + (k_{1y} - k_{2y})y_0. \end{aligned} \quad (96)$$

Thus Eq. (96) is the equation of a tilted plane for the overlap phase. The slopes of this phase plane are the components of the Wannier center. This relation is the link between the transport-aligned gauge and the later center-fixing iteration. The first line of Eq. (95) with $\mathbf{x}_0 = \mathbf{0}$ is also obtained from Eq. (35) and Eq. (51). Hence, $\{|u_{\mathbf{k}}^s\rangle\}$ generated by the adiabatic transport satisfy the minimum spread condition, in this curvature-free case.

C. Wannier Center

The above argument fixes the gauge only up to a global constant in \mathbb{K}_J and the specific value of \mathbf{x}_0 is not determined. We determine the \mathbf{x}_0 using Eqs. (69) and (70) by reconciling the slope in the interior and the jump across the boundary of the k-space.

VI. RESULTS AND DISCUSSION

The purpose of the section is to validate the formulations in the previous sections. Therefore, not only the comparison of spreads with published results but also the key equations are numerically verified with graphical representation of the results.

The calculation of the matrix elements of the projected position operators is the most important part of the procedure and there are two ways to perform it. In Secs. VIA and VIB, the relevant projected-position matrices are first evaluated directly in real space from the coordinate representation of the WFs, and the spreads are then computed from the resulting MLWFs via Eq. (106). In Sec. VIC 1, the same projected-position information is extracted in k-space from the overlap links.

These two approaches are theoretically equivalent. The former is more straightforward, whereas the latter is more computationally efficient. Thus, this section discusses not only the numerical results and the actual implementation, but also the procedural differences.

A. 1D Systems

This section focuses on verifying the formulations in 1D systems, for it allows us to see the essential parts of the formulation in simple settings.

As the solution procedure of the BFs, a scaling function method [49] with Symlet-4 [50, 51] is employed. The number of divisions in one unit cell, N , is indicated in figures and tables. As a reference for the spatial accuracy, the position eigenvectors obtained by spatially solving the eigenvalue equations of $N_C L$ -by- $N_C L$ position operator matrices are also shown [49] and denoted "Matrix" in the figures.

Since all energy bands appearing in this section do not have degeneracy, the numerical procedure begins from the eigenvalue problem described in Sec. IV.

1. Matrix elements of \hat{x}

In 1D cases, the real-space evaluation of the projected-position matrix elements $X_{s_1 s_2}$ is explicitly calculated as fol-

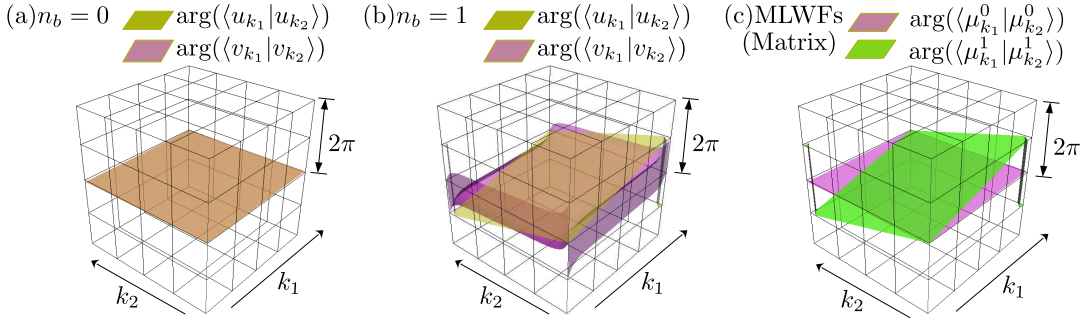


FIG. 4. (Color online) Phases of the inner products of the periodic parts of BFs. n_b denotes the band index. The axes are scaled by π . In panels (a) and (b), $\arg(\langle v_{k_1} | v_{k_2} \rangle)$ is evaluated from the raw unprocessed periodic parts and is shown as the corrugated surface (purple in the online version), whereas $\arg(\langle u_{k_1} | u_{k_2} \rangle)$ is evaluated after the transport/phase-alignment procedure and is shown as the flatter surface (yellow in the online version). Accordingly, the raw overlap phase need not be planar, while the processed overlap phase becomes approximately planar; this distinction is especially visible in panel (b), where the raw surface remains corrugated whereas the processed surface is flattened. Regions where the two semi-transparent surfaces overlap appear darker (brown in the online version). In panel (c), $|\mu_k\rangle$ denotes the periodic parts of the position eigenvectors obtained by solving the spatial position operator matrix. The band indices are denoted as the superscripts of μ , showing that the overlap phases are also approximately planar, with slopes corresponding to the Wannier centers.

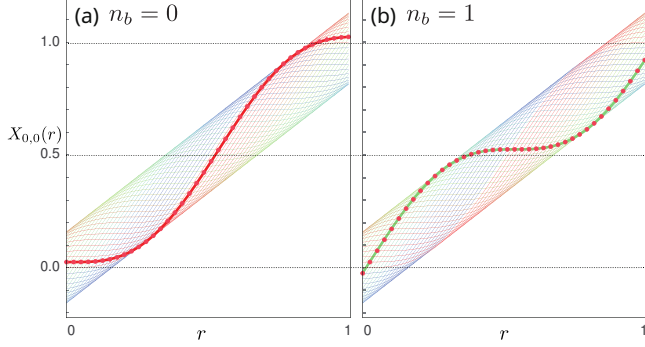


FIG. 5. (Color online) A graphical representation of Eq. (68). Thin curves, $X_{0,0}(r) = \sin 2\pi(x_0 - r)/2\pi + r$, are drawn with varying x_0 , and the thick ones are drawn with x_0 obtained through the iteration of Eqs. (69) and (70). Each dot is plotted by calculating $X_{0,0}(r) = \langle W_0(r) | \hat{x} | W_0(r) \rangle$ with the actual WFs with varying s .

TABLE I. Comparison of spreads, $\sigma_x^2 = \langle W | \{ \hat{x} - \langle W | \hat{x} | W \rangle \}^2 | W \rangle$, obtained from different methods.

Calculation condition		σ_x^2		
V_0	Band	Ref. [52]	Matrix	Current
$-0.2 \times 2\pi^2$	0	0.03	0.03	0.03
$-0.2 \times 2\pi^2$	1	0.12	0.12	0.12

lows:

$$\begin{aligned}
 \langle W_0^{s_1} | \hat{x} | W_0^{s_2} \rangle &= \langle W_0^{s_1} | \left\{ \int dx |x\rangle \langle x| \right\} \hat{x} | W_0^{s_2} \rangle \\
 &= \int \langle W_0^{s_1} | x \rangle dx x \langle x | W_0^{s_2} \rangle \\
 &= \int \overline{W_0^{s_1}}(x) x W_0^{s_2}(x) dx.
 \end{aligned} \tag{97}$$

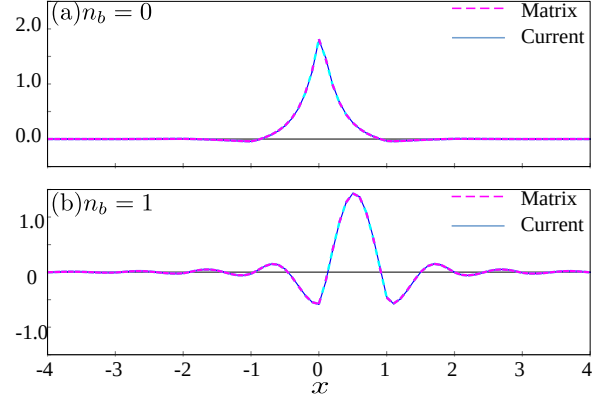


FIG. 6. (Color online) Profiles of the MLWFs. Those obtained by the current method are indicated "Current". The results indicated "Matrix" are obtained by solving the spatial position operator matrix. n_b at the left upper corner of each panel denotes the band index. In all panels, $N = 40$, $L = 200$ and $V(x) = \sum V_0 \delta(x - n)$ with $V_0 = -0.2(2\pi^2)$ [52].

In the overall algorithmic workflow, this real-space matrix is subsequently diagonalized via Eq. (55) to determine the Wannier centers. The final spreads are then evaluated from the resulting MLWFs via Eq. (106).

2. Single Band Systems

The potential energy employed is of Krönig-Penney type, $V(x) = \sum V_0 \delta(x - n)$, with $V_0 = -0.2(2\pi^2)$ [49, 52]. The spatial and k-space resolutions are $N = 40$ and $L = 200$, respectively.

As seen in Fig. 4, the overlap phase of $\langle u_{k_1}^s | u_{k_2}^s \rangle$ exhibits an approximately linear dependence on $k_1 - k_2$, indicating that the phase surface is approximately planar, consistent with

Eq. (96). The visually apparent 180° folds are simply branch cuts arising from the principal-value phase wrapping into $[-\pi, \pi)$ and do not imply any non-planarity of the underlying geometric phase surface.

Fig. 5 graphically shows the validity of Eq. (68). Although x_0 is obtained through the loop formed by Eqs. (69) and (70), the right Wannier center x_0 can also be obtained by fitting a few plots of $X_{0,0}^s$ with the sinc function.

Figure 6 shows the profiles of the MLWFs, and the curves obtained by the current method agree well with those obtained by the spatial matrix solver. The calculated minimum spreads are summarized in Table I, and the values obtained with the current method agree well with previous studies.

3. Composite Band Systems

The calculation results are compared with published results [49, 53]. The potential energy employed is of Krönig-Penney type, $V(x) = \sum V_0 \delta(x-n)$. The spatial and k-space resolutions are $N = 48$ and $L = 200$, respectively. The specific value of V_0 is indicated in the captions of Figs. 7 to 9.

As seen in Fig. 7, the overlap phase surfaces appear to be approximately planar, consistent with Eq. (96). Similar to the single-band case, the visible sharp steps are merely branch cuts due to phase wrapping modulo 2π .

As shown in Fig. 8, as in the single-band cases, the actually calculated $\{X_{0,0}^s\}$ represented by dots lie on the minimum-spread lines represented by thick curves.

Figure 9 shows the profiles of the MLWFs and the curves obtained by the current method agree well with those obtained by the spatial matrix solver, series by series. The calculated minimum spreads are listed in the Table II and those obtained by the current method are as small as the published results.

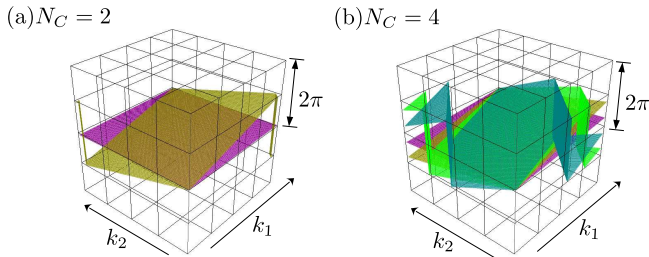


FIG. 7. (Color online) Phases of the inner products of the periodic parts of BFs. The composite band consists of #0 and #1 in panel (a), and #0 to #3 in panel (b) [53]. In panel (a), $\arg(\langle u_{k_1}^s | u_{k_2}^s \rangle)$ of series #0 and #1 of the two-band system with $V_0 = -0.661$ are plotted on k_1 - k_2 -plane. In panel (b), those of #0 to #3 with $V_0 = +0.661$ are plotted. The axes are scaled by π in the panels, and the visible folds occur when the principal value crosses $\pm\pi$ because the plotted range is restricted to $[-\pi, +\pi)$.

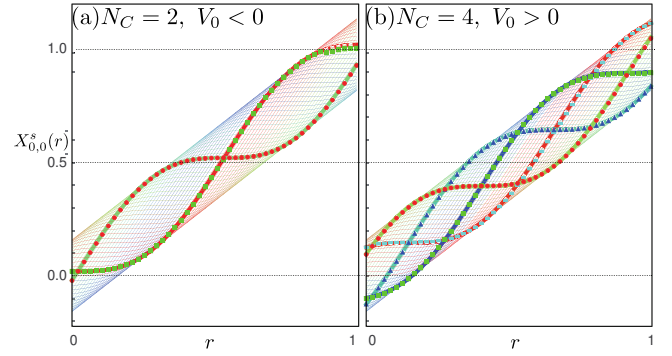


FIG. 8. (Color online) A graphical representation of Eq. (68) in composite band systems. The composite bands consist of #0 and #1 with $V_0 = 0.661$ in panel (a) and #0 to #3 with $V_0 = +0.661$ in panel (b) [53]. Thin curves, $X_{0,0}^s(r) = \sin 2\pi(x_0^s - r)/2\pi + r$, are drawn with varying x_0 . The thick ones are drawn with x_0 obtained through the iteration of Eqs. (69) and (70). Each dot is plotted by calculating $X_{0,0}^s(r) = \langle W_0^s(r) | \hat{x} | W_0^s(r) \rangle$ with the actual WFs with varying s .

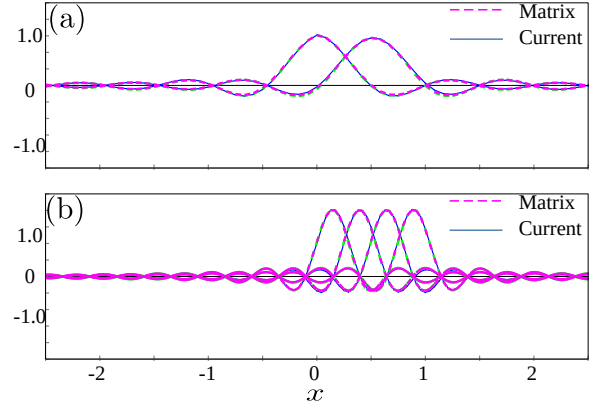


FIG. 9. (Color online) The profiles of the MLWFs in composite band systems. Those obtained by the current method are indicated "Current". The results indicated "Matrix" are obtained by solving the spatial position operator matrix. The composite band consists of #0 and #1 in panel (a), and #0 to #3 in panel (b). In both panels, the spatial and k-space resolutions are $N = 48$ and $L = 200$, respectively, and the potential energy is $V(x) = \sum V_0 \delta(x-n)$. In panel (a) $V_0 = 0.661$, and in panel (b) $V_0 = +0.661$ [53].

B. 2D Square Potential

This section presents the calculation procedures, implementation and results of a numerical model. The system consists of a unit square with a step-function-like potential well,

$$V(x,y) = \begin{cases} 1 & (x,y \in [1/2, 3/4]) \\ 0 & (\text{otherwise}). \end{cases} \quad (98)$$

The periodic boundary condition is employed on the four sides and the calculations are carried out in the unit cell and k-space both having 32×32 resolution.

TABLE II. Comparison of spreads, $\sigma_x^2 = \langle W | \{\hat{x} - \langle W | \hat{x} | W \rangle\}^2 | W \rangle$, obtained from different methods.

Calculation condition		σ_x^2		
V_0	Bands	Ref. [53]	Matrix	Current
0.661	0 to 3	0.29	0.29	0.31
-0.661	0 to 1	0.27	0.27	0.29

1. Numerical procedure

The energy bands are first peeled from each other with the following equation derived from Eq. (32):

$$|u_{\mathbf{k}+\delta\mathbf{k}}^s\rangle = \left\{ \sum_m |v_{\mathbf{k}+\delta\mathbf{k}}^m\rangle \langle v_{\mathbf{k}+\delta\mathbf{k}}^m| \right\} |u_{\mathbf{k}}^s\rangle, \quad (99)$$

with the initial condition:

$$|u_{\mathbf{k}_0}^s\rangle = |v_{\mathbf{k}_0}^s\rangle, \quad (52)$$

where, $\mathbf{k}_0 = (0, 0)$ and s indicates the peeled *energy band* (series) number.

The projection (transport) is applied outward from the center to all \mathbf{k} -points, as schematically depicted in Fig. 10. Specifically, the bases defined on the line $k_x = 0$ are transported along the k_y direction toward the boundaries at $k_x = \pm\pi$.

The directions of the transport and that of the position operator are, theoretically, desired to be consistent. In this calculation, the direction of the transport does not show any discernible effect on the results. The square-potential calculation

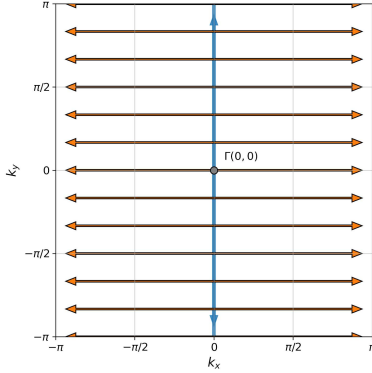


FIG. 10. (Color online) A schematic diagram of transporting the bases at the center all over the \mathbf{k} -space.

below follows the general workflow already summarized in Fig. 3. After the peeling, the following two equations are repeated alternately until a predetermined convergence criterion is met. The matrix elements are first calculated with a set of provisional WFs with $\{|u_{\mathbf{k}}^s\rangle\}$ calculated by Eq. (99),

$$\mathbf{X}^n = \langle \mathbf{W}_0(\Lambda^{n-1}) | \hat{x} | \mathbf{W}_0(\Lambda^{n-1}) \rangle. \quad (100)$$

With the estimated matrix, \mathbf{X}^n , the following eigenvalue

problem is solved,

$$\Lambda^{n+1} = \mathbf{F}^\dagger \mathbf{X}^n \mathbf{F}, \quad (101)$$

and hence the unitary matrix \mathbf{F} and the Wannier centers are obtained. As the iteration proceeds, the matrix \mathbf{X} approaches a diagonal form, namely,

$$\lim_{n \rightarrow \infty} \|\Lambda^n - \mathbf{X}^n\| \rightarrow 0, \quad (102)$$

Because of the convergent nature of the sinc-loop described in Sec. IV B 2, we use $\Lambda = \mathbf{0}$ as the initial value in the current study. For the same reason, Eq. (100) can be repeated with a convergence criterion before proceeding to Eq. (101).

Since y_0 cannot be obtained from Eq. (100) alone,

$$y_0^{s,m+1} = \langle W_0^{s,n}(x_0^{s,n}, y_0^{s,m}) | \hat{y} | W_0^{s,n}(x_0^{s,n}, y_0^{s,m}) \rangle, \quad (103)$$

is inserted to have convergence of y_0 , prior to Eq. (101).

When the convergence is reached, the series with the smallest spread is removed from the bases. From the symmetry of the system, \hat{x} is replaced with \hat{y} and the same iteration is repeated. For the final WF, Wannier center is obtained by simply repeating the single-element version of Eq. (100).

2. Peeling

The left half of Fig. 11 shows the energy bands obtained by solving the Schrödinger equation of the system. The right half shows the peeled *energy bands* defined as follows:

$$e_{\mathbf{k}}^s = \sum_n |\langle u_{\mathbf{k}}^s | v_{\mathbf{k}}^n \rangle|^2 \varepsilon_{\mathbf{k}}^n, \quad (104)$$

where $\varepsilon_{\mathbf{k}}^n$ is the original energy as a function of the energy band index n and the wavenumber \mathbf{k} . As circled in Fig. 11, the original energy band curvatures have rather abrupt folds, for the band numbering is simply done according to the magnitude of the local energy in the \mathbf{k} -space. After performing the procedure described by Eq. (99), the folds disappear by *naturally* connecting and bending the original energy band curvatures. This is only for visualization of the effect of the adiabatic transport, and the reconstruction of the band curvature per se does not have any effect on the calculation of the spread.

The significance of Eq. (99) is also seen in the discrete curl of the diagonal connection $\mathbf{A}_{\mathbf{k}}^s = -i \langle u_{\mathbf{k}}^s | \nabla_{\mathbf{k}} | u_{\mathbf{k}}^s \rangle$ evaluated on the original and processed periodic parts of the BFs, namely $\{|v_{\mathbf{k}}^n\rangle\}$ and $\{|u_{\mathbf{k}}^s\rangle\}$, as shown in Fig. 12. Here, this quantity is used solely as a frame-smoothness diagnostic.

For a smoothly tracked nondegenerate Hamiltonian eigenband in a spinless \mathcal{PT} -symmetric system, the gauge-invariant Abelian Berry curvature vanishes pointwise wherever it is defined [54, 55]. The quantities shown in Figs. 12 and 17 are not intended to represent the physical Berry curvature. Before transport (Fig. 12(a)), the raw energy-ordered frame changes discontinuously near internal band intertwinings, and the discrete curl of the diagonal connection is contaminated by band-index switching artifacts. After transport (Fig. 12(b)), the curl

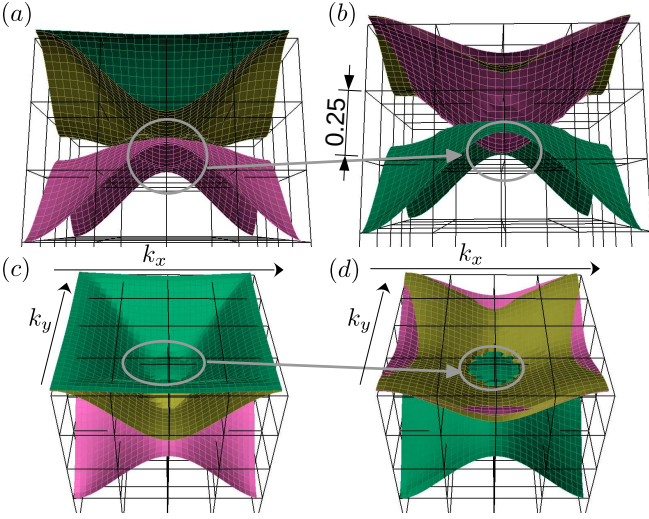


FIG. 11. (Color online) Energy bands #3, #4 and #5 of the 2D square potential system ($L=36$). The left half shows the original energy bands and the right half shows adiabatically peeled *energy bands*. Strong bends are observed in the circled parts of the original energy band curvatures on the left side, while the bends are relaxed by the adiabatic transport via connecting multiple numbers of the original curvatures.

of the diagonal connection becomes approximately zero in the interior, confirming a smooth transported frame. The residual finite values strictly localized near the boundary are the geometric seam defects of the transported frame, which is consistent with the exact diagnostics (ω_β^1 and σ_{\min}) analyzed later in Section VIC.

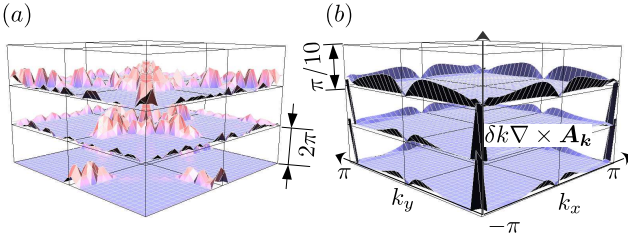


FIG. 12. (Color online) Scaled curls of the diagonal connection (used here as frame-smoothness diagnostics) of the square potential model ($L=36$), defined as $\delta k |\nabla \times \mathbf{A}_k|$, where \mathbf{A}_k denotes the corresponding diagonal connection of the frame being plotted, before and after the adiabatic transport. A scale factor of 40 is applied to the smoother low-amplitude diagnostic surface obtained after transport so that it can be shown alongside the rough high-amplitude diagnostic surface before transport in the same figure; these two surfaces are distinguished by color in the online version. After realigning the original Bloch frames, the curl of the diagonal connection becomes approximately zero in the interior, while finite values remain on the boundary seam. Most of the rough pre-transport variations in this case are caused by the intertwining of the locally energy-ordered bands.

3. Solving the Position Eigenvalue Problem and Identifying the Wannier Center

Following the adiabatic transport, the iteration based on Eqs. (100) and (101) is applied. The purpose of the following phase plot is to verify the phase-plane relation in Eq. (96) in two dimensions. The second lines of Eqs. (95) and (96) are precisely the component form used in this numerical plot. As seen in Fig. 13, the processed overlap phase is well approximated by this planar surface. The visible folds are artifacts of the principal-value wrapping of the phase into $[-\pi, \pi)$ and do not indicate a breakdown of the underlying phase-plane relation. The same behavior is observed when the roles of k_x and k_y are interchanged.

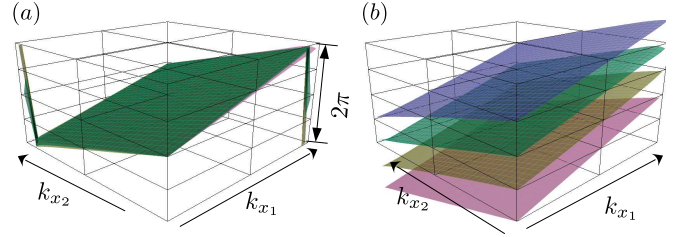


FIG. 13. (Color online) Phase of the overlap $\langle u_{\mathbf{k}_1}^s | u_{\mathbf{k}_2}^s \rangle$ with fixed k_y for the square potential model ($L=36$). The figure on the left side shows the three overlap-phase surfaces of the three MLWFs with $k_y = 0$. They are approximately the same plane, since all three MLWFs share the same Wannier center $\mathbf{x}_0 = (1/2, 1/2)$ as the slope indicates. The visible folds occur when the principal value crosses $\pm\pi$, because the plotted range is restricted to $[-\pi, +\pi)$. The four surfaces on the right side correspond to one of the MLWFs at $k_y = -\pi, -\pi/2, 0, +\pi/2$, respectively. To show them distinctively, the planes are elevated and separated by $\pi/4$, even though they are essentially the same plane.

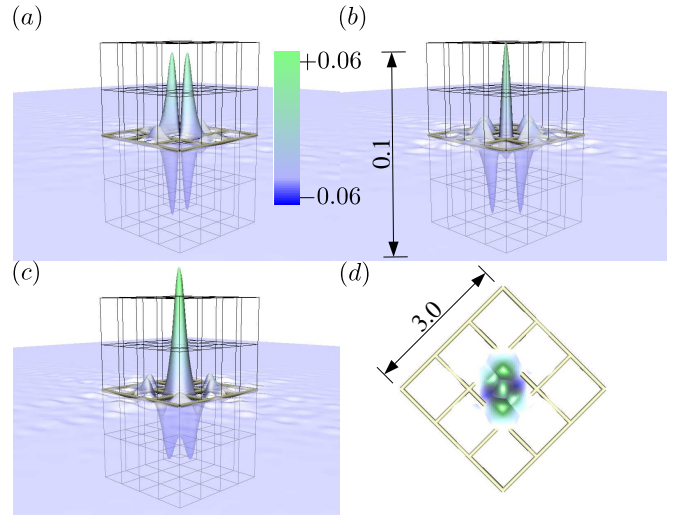


FIG. 14. (Color online) The three MLWFs are shown in panels (a), (b) and (c). To show the negative parts of the MLWFs, they are drawn with transparent surfaces. Panel (d) shows all three MLWFs. The white rectangle objects are added to indicate 3×3 unit cells.

TABLE III. Wannier Centers and Spreads of Square Potential Model.

Series#	x_0	y_0	σ_s^2
1	0.50	0.50	0.24
2	0.50	0.50	0.24
3	0.50	0.50	0.28

Figure 14 shows the MLWFs obtained from the periodic parts and the Wannier centers. The MLWFs in Fig. 14(a),(b) and (c) are solutions of the following equations,

$$\begin{aligned}\hat{x}|W_0^a\rangle &= x_0|W_0^a\rangle \\ \hat{y}|W_0^b\rangle &= y_0|W_0^b\rangle \\ (\hat{x} + \hat{y})|W_0^c\rangle &= c_0|W_0^c\rangle.\end{aligned}\quad (105)$$

Since they have the same Wannier centers, it is possible to achieve stronger localization by linearly combining some of them, although it is not pursued in the current study.

The spatial calculation of Wannier centers and the spreads are defined by the following equations,

$$\begin{aligned}\mathbf{x}_0 &= \langle W_0^s | \hat{\mathbf{x}} | W_0^s \rangle \\ \sigma_s^2 &= \langle W_0^s | (\hat{\mathbf{x}} - \mathbf{x}_0)^2 | W_0^s \rangle,\end{aligned}\quad (106)$$

and the results are listed in Table III.

C. Graphene

This section focuses on MLWFs of graphene. The entire calculation is performed in the oblique coordinate system and hence the coordinate (ξ, η) is transformed to (x, y) ,

$$\begin{pmatrix} x \\ y \end{pmatrix} = \begin{pmatrix} 1 & -1/2 \\ 0 & \sqrt{3}/2 \end{pmatrix} \begin{pmatrix} \xi \\ \eta \end{pmatrix}.\quad (107)$$

The wavenumbers are also in the oblique coordinate system and denoted (k_ξ, k_η) . The final spreads and Wannier centers are presented in the Cartesian coordinate system.

First-principles calculations were carried out using QUANTUM ESPRESSO (QE) [56–58]. The spatial resolutions were set identical to the k-space resolutions. The calculations are carried out by changing the resolution from 12×12 to 36×36 in the k-space; the corresponding centers and spreads are summarized later in Table IV. The link variables were taken as the raw nearest-neighbor overlaps $\langle v_{\mathbf{k}}^m | v_{\mathbf{k} + \delta \mathbf{k}_\alpha}^n \rangle$ provided by the WANNIER90 (W90) [13, 14, 59] interface, where $\delta \mathbf{k}_\alpha$ connects a mesh point to its near neighbors (see Appendix F for notation). These links are used to evaluate the matrix elements of the position operators, as shown later in this section.

As a setting of the QE calculation, we choose five Wannier functions consisting of two $C - p_z$ orbitals (π manifold) and three bond-centered orbitals (σ bonds), providing a minimal chemically-motivated set for graphene within the five-band subspace used to build the overlap matrices (see Appendix E

for details).

While five energy bands, from #0 to #4 are provided to the W90, lower four energy bands, #0 to #3, are fed into the current computational program. Eventually, three MLWFs are obtained both from W90 and the current program.

In the case of graphene, the chosen sequential extraction from the composite subspace isolates a component that inevitably accumulates a topologically obstructed intermediate state. Therefore, the specific 4-band pruning and deflation sequence detailed in Fig. 15 is devised to execute the ‘‘More MLWF?’’ loop of the general flowchart (Fig. 3).

The calculation results are presented in this section and the spreads are compared with those obtained from W90 under the very same conditions to check the validity and utility of the current method.

1. Matrix elements of \hat{x}

Instead of using BFs of graphene, the links, $\{\langle v_{\mathbf{k}_1}^{n_1} | v_{\mathbf{k}_2}^{n_2} \rangle\}$, generated by W90 are utilized. By using the links, the calculation of the matrix elements of the position operator, for example, are performed as follows:

$$\begin{aligned}\langle W_0^{s_1} | \hat{x} | W_0^{s_2} \rangle &= \frac{1}{L^2} \sum_{\mathbf{k}_1, \mathbf{k}_2} \langle u_{\mathbf{k}_1}^{s_1} | e^{-i\mathbf{k}_1 \cdot \hat{\mathbf{x}}} e^{i\mathbf{k}_2 \cdot \hat{\mathbf{x}}} | u_{\mathbf{k}_2}^{s_2} \rangle \\ &= i \sum_{\mathbf{k}_1, \mathbf{k}_2} \langle u_{\mathbf{k}_1}^{s_1} | \partial_{k_x} | u_{\mathbf{k}_2}^{s_2} \rangle \delta_{\mathbf{k}_1, \mathbf{k}_2} \\ &= i \sum_{\mathbf{k}} \langle u_{\mathbf{k}}^{s_1} | \partial_{k_x} | u_{\mathbf{k}}^{s_2} \rangle \\ &= \frac{i}{2\delta k} \sum_{\mathbf{k}} \left\{ \langle u_{(k_x, k_y)}^{s_1} | u_{(k_x + \delta k, k_y)}^{s_2} \rangle - \langle u_{(k_x, k_y)}^{s_1} | u_{(k_x - \delta k, k_y)}^{s_2} \rangle \right\} \\ &= \frac{i}{2\delta k} \sum_{\mathbf{k}, n_1, n_2} \bar{f}_{(k_x, k_y)}^{s_1, n_1} \left\{ \langle v_{(k_x, k_y)}^{n_1} | v_{(k_x + \delta k, k_y)}^{n_2} \rangle f_{(k_x + \delta k, k_y)}^{s_2, n_2} \right. \\ &\quad \left. - \langle v_{(k_x, k_y)}^{n_1} | v_{(k_x - \delta k, k_y)}^{n_2} \rangle f_{(k_x - \delta k, k_y)}^{s_2, n_2} \right\} \\ &\quad + \mathcal{O}(\delta k^2)\end{aligned}\quad (108)$$

At the very beginning of the calculation, the basis vectors are expressed as,

$$\begin{aligned}f_{\mathbf{k}}^0 &= \{1, 0, 0, \dots, 0\} \\ f_{\mathbf{k}}^1 &= \{0, 1, 0, \dots, 0\} \\ &\vdots \\ f_{\mathbf{k}}^{N_C-1} &= \{0, 0, 0, \dots, 1\},\end{aligned}\quad (109)$$

for all \mathbf{k} , in place of $\langle x | v_{\mathbf{k}}^n \rangle$. Every matrix transformation is done on the bases $\{f_{\mathbf{k}}^n\}$, and the inner product must always be done with the links, as seen in Eq. (108).

2. Peeling

In the graphene calculation, the initial condition in Eq. (52) is imposed at $\mathbf{k}_0 = (\pi, \pi)$ in the oblique reciprocal coordinates (k_ξ, k_η) . This choice fixes the initial local frame used for the adiabatic transport. It is different from the initial value of the Wannier-center parameters, which is set to $\mathbf{\Lambda} = \mathbf{0}$ in the center-fixing update described below.

The left half of Fig. 16 shows the energy bands obtained from W90. The right half shows the peeled *energy bands* defined by Eq. (104). As circled in Fig. 16, the original

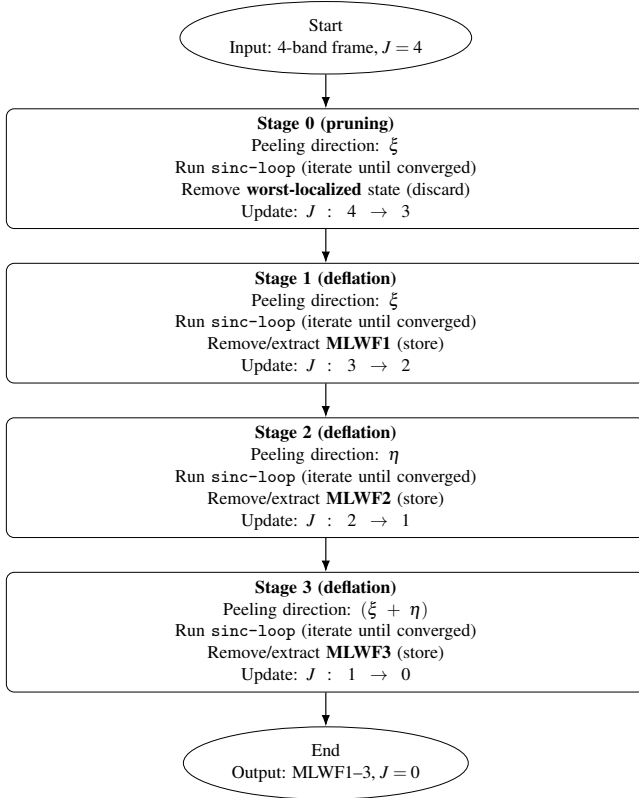


FIG. 15. Flowchart of the 4-band peeling/deflation procedure used for graphene. Stage 0 (pruning): ξ -direction peeling and the sinc-loop, then discard the least localized state ($J : 4 \rightarrow 3$). Stages 1–3 (deflation): repeat peeling and the sinc-loop, then extract/store MLWF1–3 sequentially using the ξ , η , and $(\xi + \eta)$ directions ($J : 3 \rightarrow 2 \rightarrow 1 \rightarrow 0$).

energy band curvatures have rather abrupt folds, for the band numbering is simply done according to the magnitude of the local energy in the \mathbf{k} -space. After performing the procedure described by Eq. (99), the folds disappear by *naturally* connecting and bending the original energy band curvatures.

The significance of Eq. (99) is seen in the discrete curl of the diagonal connection calculated with the original and processed periodic parts of the BFs, namely $\{|v_k^n\rangle\}$ and $\{|u_k^s\rangle\}$, as shown in Fig. 17. As in the square-potential case, this diagnostic is not the gauge-invariant physical Berry curvature of a smoothly tracked Hamiltonian eigenband. In the present spinless \mathcal{PT} -symmetric setting, that physical curvature van-

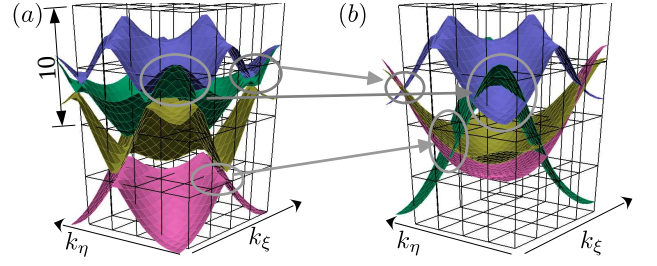


FIG. 16. (Color online) Energy band #0 to #4 of graphene ($L=22$). The left half shows the original energy bands and the right half shows adiabatically peeled *energy bands*. Strong bends are observed in the circled parts of the original energy band curvatures on the left side, while the bends are relaxed by the adiabatic transport via connecting multiple numbers of the original curvatures. (k_ξ, k_η) -axis corresponds to the oblique reciprocal coordinate spanning the primitive parallelogram cell $[-\pi, \pi)$, rather than a conventional high-symmetry path (such as Γ -M-K- Γ) in the hexagonal Brillouin zone.

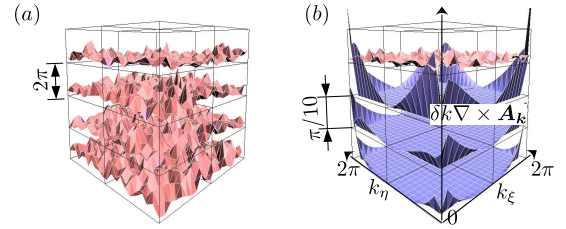


FIG. 17. (Color online) Scaled curls of the diagonal connection (used here as frame-smoothness diagnostics) of graphene ($L=22$), defined as $\delta k |\nabla \times \mathbf{A}_k|$, where \mathbf{A}_k denotes the corresponding diagonal connection of the frame being plotted, before and after the adiabatic transport. A factor of 40 is applied to the smoother low-amplitude diagnostic surface in panel (b) so that it can be shown together with the rough high-amplitude diagnostic surface in panel (a); these two surfaces are distinguished by color in the online version. In panel (a), the diagnostic is rough throughout the Brillouin zone because the raw energy-ordered frame is globally affected by band intertings across the composite subspace. In panel (b), it becomes nearly zero in the interior for the lower three peeled series, while finite variations remain on the boundary seam. These seam-localized variations are the boundary gauge defects analyzed later in Figs. 22–24.

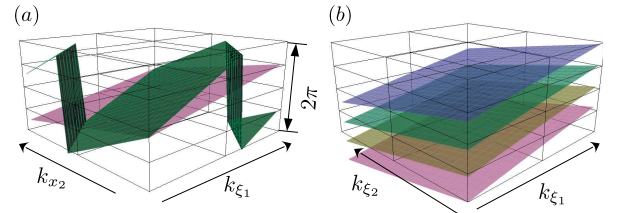


FIG. 18. (Color online) Phase of the overlap of graphene ($L=22$), $\langle u_{k_1}^s | u_{k_2}^s \rangle$, with fixed k_η . The figure on the left side shows the three overlap-phase surfaces of the three MLWFs with $k_\eta = 0$. The slopes reflect ξ_0 s of the corresponding MLWFs. The Wannier centers correspond to $\xi_0 = 1/3, 5/6, 5/6$. The visible folds occur when the principal value crosses $\pm\pi$, because the plotted range is restricted to $[-\pi, +\pi)$. The four surfaces on the right correspond to one of the MLWFs at $k_\eta = -\pi, -\pi/2, 0, +\pi/2$, respectively. To show them distinctively, the planes are elevated and separated by $\pi/4$, although they are essentially the same plane.

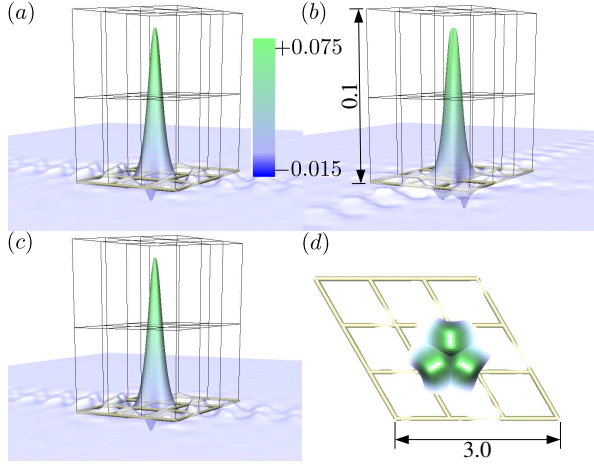


FIG. 19. (Color online) MLWFs of graphene ($L=22$). The three MLWFs are shown in panels (a), (b) and (c). To show the negative parts of the MLWFs, they are drawn with transparent surfaces. Panel (d) shows all three MLWFs together. The rectangular objects (gold-colored in the online version) are added to indicate 3×3 unit cells. The Wannier centers of the MLWFs seen in panels (a),(b) and (c) are $(0.25, 0.15)$, $(0.50, 0.58)$ and $(0.75, 0.14)$, respectively.

TABLE IV. Centers aligned by matching (row permutation only). Units: Å. Values rounded to two decimals.

L	WF#	Current			W90		
		Ω (Å ²)	x_0 (Å)	y_0 (Å)	Ω (Å ²)	x_0 (Å)	y_0 (Å)
12	1	0.86	-0.62	-0.35	1.15	-0.63	-0.36
	2	1.06	0.00	0.71	1.58	0.01	0.72
	3	1.26	0.62	-0.35	0.92	0.62	-0.36
22	1	1.16	-0.62	-0.35	0.91	-0.63	-0.36
	2	1.58	0.00	0.72	0.99	0.00	0.72
	3	1.91	0.62	-0.37	1.03	0.63	-0.36
30	1	1.43	-0.62	-0.35	1.47	-0.63	-0.36
	2	1.99	0.00	0.72	1.48	0.00	0.72
	3	2.47	0.62	-0.37	1.49	0.63	-0.36

ishes pointwise. Before transport, the raw energy-ordered frame is globally affected by band interwindings across the composite subspace, so the corresponding diagnostic appears rough throughout the Brillouin zone. After transport, the diagnostic becomes nearly zero in the interior of the Brillouin zone, whereas finite $\mathcal{O}(L^0)$ variations remain concentrated on the boundary seam. Those seam-localized variations are precisely the geometric defects quantified later by $\omega_\beta^1(\mathbf{k})$ and $\sigma_{\min}(\mathbf{k}; \delta\mathbf{k}_\beta)$.

3. Obtained MLWFs and their Wannier Centers

Following the adiabatic transport, the iteration based on Eqs. (100) and (101) is applied. The same phase-plane in-

terpretation applies to graphene, but now in the oblique coordinates used for the honeycomb lattice. Namely, the second line of Eq. (96) is read with $(k_x, k_y; x_0, y_0)$ replaced by $(k_\xi, k_\eta; \xi_0, \eta_0)$. As seen in Fig. 18, the processed overlap phase is well approximated by this planar surface. The visible folds are artifacts of principal-value phase wrapping. The same behavior is observed when the roles of k_ξ and k_η are interchanged. Hence the slopes of the phase plane give the individual components of $\xi_0 = (\xi_0, \eta_0)$.

Figure 19 shows the MLWFs obtained from the periodic parts and the Wannier centers. The WFs in Fig. 19(a)–(c) are solutions of the following equations,

$$\begin{aligned} \hat{\eta}|W_0^a\rangle &= \eta_0|W_0^a\rangle \\ \hat{\xi}|W_0^b\rangle &= \xi_0|W_0^b\rangle \\ (\hat{\xi} + \hat{\eta})|W_0^c\rangle &= \zeta_0|W_0^c\rangle \end{aligned} \quad (110)$$

The 4-band pruning/deflation sequence used for graphene is summarized in Fig. 15.

4. Practical convergence of the center-fixing update

We briefly record the practical convergence behavior of the center-fixing updates used in the graphene calculation. The center update is not a minimization of the spread functional, but a fixed-point/self-consistent solution of the projected-position matrix elements and the associated Wannier-center parameters. Here J denotes the number of remaining branches in the pruning/deflation sequence. In the calculations shown here, the center parameters are initialized by $\Lambda = 0$. For the branch-center update, convergence is monitored by the squared displacement in the underlying (ξ_0, η_0) variables,

$$\Delta_{\xi\eta}^2 = (\xi_0^{(n+1)} - \xi_0^{(n)})^2 + (\eta_0^{(n+1)} - \eta_0^{(n)})^2.$$

In the implementation used for Fig. 20, the branch update is iterated until $\Delta_{\xi\eta}^2 < 10^{-8}$, with at least five iterations imposed to avoid premature termination.

Figure 20 shows a representative $L = 22$ graphene run for the $J = 4, 3, 2$ stages, together with the mesh dependence of the selected $J = 3$ branch corresponding to MLWF1. For the $L = 22$ run, the highlighted precursor branch at the $J = 4$ stage, the MLWF1 branch at the $J = 3$ stage, and the MLWF2 branch at the $J = 2$ stage terminate after 14, 6, and 5 plotted iteration points, respectively. The final $J = 1$ step yields MLWF3 and is omitted from the figure for compactness; it is a single-branch update and also converges within five iterations. For $L = 12, 18, 20, 22, 26, 30$, and 36, the final values of the selected $J = 3$ MLWF1 branch remain nearly unchanged, $x_0 = 0.2483$ – 0.2512 and $y_0 = 0.1403$ – 0.1416 in the plotted coordinate convention. Thus the center update is stable with respect to mesh refinement in this isolated graphene composite-band subspace. For stronger internal degeneracies, or when projected-position eigenvalues become nearly degenerate, branch assignment may require additional checks. The separate problem of selecting an optimal subspace from ener-

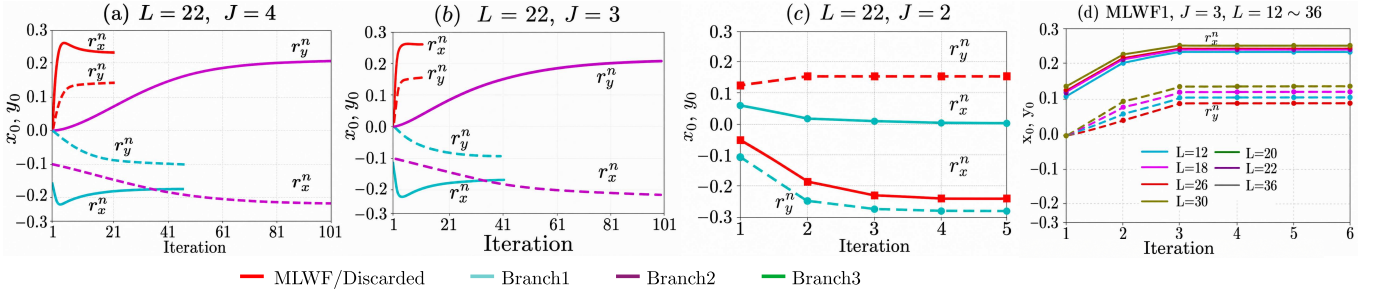


FIG. 20. (Color online) Practical convergence of the center-fixing updates in graphene. The four panels, from left to right, show the iteration trajectories of (x_0, y_0) for a representative $L = 22$ run at the successive $J = 4, 3, 2$ stages of the pruning/deflation sequence, followed by the mesh dependence of the selected $J = 3$ branch corresponding to MLWF1. Here J denotes the number of remaining branches in the composite subspace. Throughout the figure, solid and dashed curves denote x_0 and y_0 , respectively. In the first three panels, the red curves indicate, respectively, the precursor branch removed at the $J = 4$ stage, the MLWF1 branch selected at the $J = 3$ stage, and the MLWF2 branch selected at the $J = 2$ stage. In panels (a) and (b), markers are omitted because the trajectories are too dense for marker symbols to be helpful. In the rightmost panel, the selected $J = 3$ MLWF1 branch is shown for $L = 12, 18, 20, 22, 26, 30$, and 36 ; colors distinguish L , while the same solid/dashed convention distinguishes x_0 and y_0 . The horizontal axis is the iteration count actually performed. No interpolation or artificial extension of the trajectories is used. The plotted coordinates are the dimensionless transformed coordinates $(x_0, y_0) = (\xi_0 - \eta_0/2, \sqrt{3}\eta_0/2)$, not real-space Wannier-center coordinates in units of \AA . The selected MLWF1 center remains nearly unchanged over the full range of mesh sizes.

getically entangled bands is outside the scope of the present work.

5. Spreads and reciprocal-space diagnostics

The obtained centers and spreads are compared with those from W90 in Table IV. Figure 21 compares the spreads of the graphene MLWFs as a function of L . The spreads obtained from the real-space integration (squares) and from the reciprocal-space finite-difference functional [10, 13, 14] (circles; see Appendix F) agree well with those from W90, thereby confirming the validity of the adiabatic transport, projected position operator eigenvectors, sinc-loop and the pruning/deflation workflow.

Although the orbital shapes and Wannier centers agree well with those from W90, the spreads increase approximately linearly with L as shown in Fig. 21. This resolution dependence is understood by following the procedures shown in Fig. 15 one-by-one.

(i) $J = 4 \rightarrow 3$. Starting from the four-band subspace, we diagonalize $\hat{\xi}$ and remove the least localized state. At this stage, as seen in Figs. 24(b) and (f), the transported $J = 3$ subspace becomes smooth in both link directions, as $\sigma_{\min}(\mathbf{k}; \delta \mathbf{k}_\beta)$, a measure of the closeness of adjacent local spaces spanned by $\{|u_{\mathbf{k}}^s\rangle\}$ (see Appendix F), is nearly flat and close to unity throughout the Brillouin zone. Thus, the neighboring local subspaces spanned by $\{|u_{\mathbf{k}}^s\rangle\}$ are almost identical. This $\sigma_{\min} \approx 1$ behavior serves as the direct visual confirmation of Eq. (36).

(ii) $J = 3 \rightarrow 2$. After MLWF1 is extracted, the seam is exposed and two complementary diagnostics become relevant. For the extracted series $s = 1$, we define the diagonal link

$$m_\beta^1(\mathbf{k}) = \langle u_{\mathbf{k}}^1 | u_{\mathbf{k}+\delta \mathbf{k}_\beta}^1 \rangle, \quad (111)$$

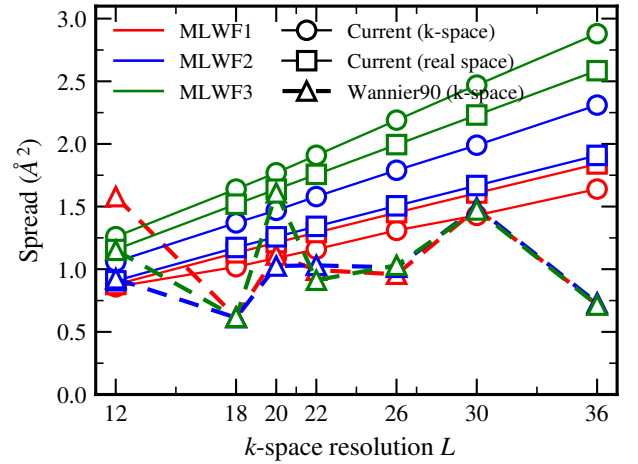


FIG. 21. (Color online) Spreads of the three graphene MLWFs as a function of the k -mesh resolution L . Squares: results of the present method evaluated in real space via Eq. (106). Circles: results of the present method evaluated in reciprocal space from the link matrices. Triangles: WANNIER90 results evaluated in reciprocal space from the same link matrices.

and its singular value $\sigma_\beta^1(\mathbf{k}) = |m_\beta^1(\mathbf{k})|$. Because this is a 1×1 overlap matrix, σ_β^1 is simply the absolute value of the link itself. We then define the corresponding single-state kernel

$$\omega_\beta^1(\mathbf{k}) = 1 - [\sigma_\beta^1(\mathbf{k})]^2 = 1 - |m_\beta^1(\mathbf{k})|^2. \quad (112)$$

Figure 22 shows that $\omega_\beta^1(\mathbf{k})$ is concentrated on the boundary seam, while Fig. 23(a) shows that its representative maximum value remains strictly constant as L is increased, thus $\omega_\beta^1(\mathbf{k}) \sim$

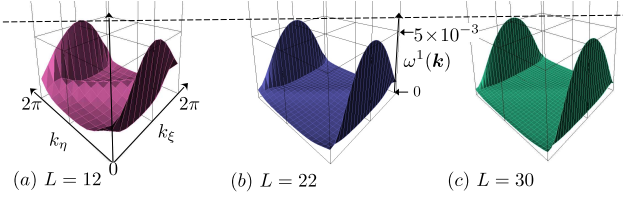


FIG. 22. (Color online) Single-state geometric defect $\omega_\beta^1(\mathbf{k})$ carried by the extracted MLWF1 in graphene. This quantity is defined as $\omega_\beta^1(\mathbf{k}) = 1 - |\langle u_{\mathbf{k}}^1 | u_{\mathbf{k}+\delta\mathbf{k}_\beta}^1 \rangle|^2$, isolating the geometric distortion of the one-dimensional subspace along the link direction β . Panels (a)–(c) display its distribution in the oblique reciprocal coordinates (k_ξ, k_η) for mesh resolutions $L = 12, 22,$ and 30 .

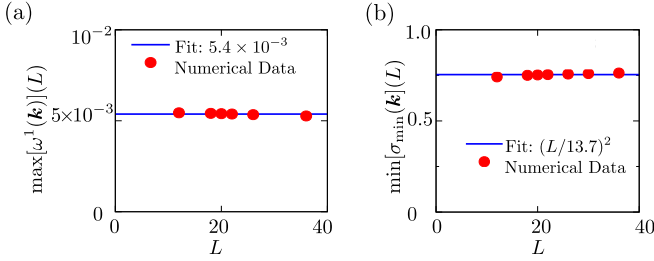


FIG. 23. (Color online) Resolution dependence of the local geometric defects on the boundary seam in graphene. (a) The maximum value of the single-state spread kernel carried by MLWF1, $\max_{\mathbf{k}} \omega_\beta^1(\mathbf{k})$, plotted against the mesh resolution L . (b) The absolute minimum of the subspace-level diagnostic, $\min_{\mathbf{k}} \sigma_{\min}(\mathbf{k}; \delta\mathbf{k}_\beta)$, for the residual $J = 2$ subspace. Both quantities appear L -independent, providing direct numerical evidence that the local gauge mismatch on the seam remains an $\mathcal{O}(L^0)$ geometric constant.

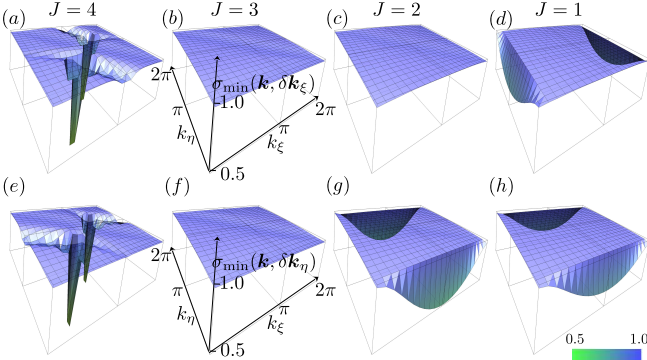


FIG. 24. (Color online) Principal-angle diagnostic $\sigma_{\min}(\mathbf{k}; \delta\mathbf{k}_\alpha)$ of the transported subspaces in graphene ($L = 22$). The upper panels (a)–(d) show the diagnostic evaluated along the ξ -direction ($\alpha = \xi$), while the lower panels (e)–(h) show it along the η -direction ($\alpha = \eta$). The initial transported $J = 3$ subspace is globally flat near unity in both directions. After extracting MLWF1, the residual $J = 2$ subspace remains flat along ξ but exhibits broad dog-ear-like depressions near the boundaries along η .

$\mathcal{O}(L^0)$ on the boundary.

The residual $J = 2$ subspace left behind after the extraction shows the same seam geometry at the subspace level. As visualized in Fig. 24(c), it stays approximately level in the k_ξ -direction, faithfully preserving the 1D uniformity mandated by Eq. (36). However, it inevitably develops dog-ear-like cliffs in k_η -direction along the boundary seam, as Fig. 24(g) clearly illustrates where the geometric frustration is concentrated. The magnitude of this geometric defect is measured by the floor of $\sigma_{\min}(\mathbf{k}; \delta\mathbf{k}_\beta)$, which is likewise L -independent and of the order of $\mathcal{O}(L^0)$, as explicitly shown in Fig. 23(b).

The linear growth of the total spread Ω^1 is therefore not caused by a local divergence of the spread kernel. Rather, what grows with L is the macroscopic number of seam links that carry this finite defect. Using the discrete reciprocal-space measure $\nu_\beta = w_\beta/N_{\mathbf{k}}$ introduced in Appendix F, the seam contribution to the spread is estimated as

$$\Delta\Omega_{\text{seam}}^1 \sim \sum_{\mathbf{k} \in \text{seam}} \nu_\beta \omega_\beta^1(\mathbf{k}). \quad (113)$$

On a uniform $L \times L$ mesh, the discrete measure evaluates to $\nu_\beta = \mathcal{O}(L^0)$, and the number of grid points along the 1D boundary seam is $\#\{\mathbf{k} \in \text{seam}\} = \mathcal{O}(L)$. As rigorously evaluated in Appendix F4 and shown in Fig. 23, both the single-state and subspace-level diagnostics remain strictly finite ($\mathcal{O}(L^0)$) on this seam. Thus, the macroscopic integration strictly yields a linear divergence:

$$\Delta\Omega_{\text{seam}}^1 = \mathcal{O}(L). \quad (114)$$

The observed scaling in Fig. 21 is therefore a geometric consequence of a boundary-supported $\mathcal{O}(L^0)$ mismatch accumulated over an $\mathcal{O}(L)$ seam, not a numerical artifact. Ultimately, this $\mathcal{O}(L)$ spread scaling is an intrinsic physical signature of the 2D gauge frustration stemming from the non-commutativity of the projected position operators [10, 32]. As originally established by MV, iterative minimization schemes handle this non-commutativity variationally—distributing the geometric incompatibility globally across all reciprocal directions to achieve a minimum total spread [10]. In stark contrast, our deterministic sequential extraction mathematically forces the gauge to be flat along the chosen one-dimensional strings. This strict 1D flattening inevitably sweeps the entire geometric frustration into the 1D boundary seams, manifesting perfectly as the $\mathcal{O}(L)$ scaling. While subsequent multi-dimensional iterative optimization [10, 13] could be applied to redistribute this concentrated defect and reduce the total spread, isolating this exact geometric manifestation falls precisely within the scope of our constructive and analytical framework.

VII. SUMMARY

We proposed a non-variational constructive algorithm to build maximally localized Wannier functions (MLWFs) that unifies gauge smoothing and the eigenvalue problem of the projected position operator into a single deterministic frame-

work. Rather than treating gauge alignment and center determination as separate steps or minimizing the spread functional over the gauge manifold, we demonstrated that discrete Kato parallel transport across band degeneracies emerges naturally as an integral part of the solution procedure for the position eigenvectors.

By directly aligning the periodic parts of the Bloch functions, this transport suppresses band-index swaps and approximately linearizes the overlap phase in the interior of the Brillouin zone. Operating within this transport-aligned gauge, we introduced a sinc-kernel transformation that maps the Wannier center search to deterministic fixed-point iterations and self-consistent updates for explicit center equations and projected-position matrices, rather than spread-functional minimization over the gauge manifold.

Benchmarks on 1D models, a 2D square potential, and graphene yield Wannier centers and orbital shapes in good agreement with standard gradient-based minimization (e.g., W90). Furthermore, because our sequential extraction works to flatten the interior gauge instead of globally distributing the geometric mismatch, it transparently isolates the physical origin of the $\mathcal{O}(L)$ spread growth observed in graphene. The finite $\mathcal{O}(L^0)$ local defects accumulated on the one-dimensional boundary seam strictly integrate to an $\mathcal{O}(L)$ macroscopic spread growth. This confirms that the resolution-dependent spread divergence is an intrinsic geometric manifestation of non-commuting projected position operators. Remaining challenges include addressing the non-uniqueness of projection directions for co-centered WFs and managing directional incompatibilities during multi-step extractions.

ACKNOWLEDGMENTS

This work was supported by JSPS KAKENHI (Grants No. JP25K01609, No. JP22H05473, and No. JP21H01019), JST CREST (Grant No. JPMJCR19T1). K.W. acknowledges the financial support for Basic Science Research Projects (Grant No. 2401203) from the Sumitomo Foundation and a special individual research fund from Kwansai Gakuin University.

Appendix A: Supplemental Calculation for Adiabatic Expansion

The eigenvalue equation of the system is defined as follows:

$$\hat{H}(k)|v_{\mathbf{k}}^n\rangle = \varepsilon^n(t)|v_{\mathbf{k}}^n\rangle, \quad (\text{A1})$$

where $\varepsilon_n(t)$ is the instantaneous eigenvalue of the Bloch Hamiltonian. The transient solution of the system satisfies the following equation:

$$i\hbar \frac{d}{dt} |\Psi(t)\rangle = \hat{H}(k) |\Psi(t)\rangle, \quad (\text{A2})$$

where the solution is decomposed into the instantaneous eigenstates of the system:

$$|\Psi(t)\rangle = \sum_n c_{\mathbf{k}}^n(t) e^{-i\theta^n(t)} |v_{\mathbf{k}}^n\rangle, \quad (\text{A3})$$

where,

$$\theta^n(t) = \frac{1}{\hbar} \int^t \varepsilon^n(\tau) d\tau. \quad (\text{A4})$$

The time derivative of $|\Psi(t)\rangle$ is calculated in two ways:

$$\begin{aligned} \frac{d}{dt} |\Psi(t)\rangle &= \sum_n \left\{ \frac{dc_{\mathbf{k}}^n}{dt}(t) |v_{\mathbf{k}}^n\rangle - \frac{i}{\hbar} c_{\mathbf{k}}^n(t) \varepsilon_n(t) |v_{\mathbf{k}}^n\rangle + c_{\mathbf{k}}^n \frac{d}{dt} |v_{\mathbf{k}}^n\rangle \right\} e^{-i\theta^n(t)} \\ \frac{d}{dt} |\Psi(t)\rangle &= -\frac{i}{\hbar} \sum_n c_{\mathbf{k}}^n \varepsilon_n |v_{\mathbf{k}}^n\rangle e^{-i\theta^n(t)}. \end{aligned} \quad (\text{A5})$$

Hence, we obtain the equation for $c_{\mathbf{k}}^n$:

$$\sum_n \frac{dc_{\mathbf{k}}^n}{dt}(t) |v_{\mathbf{k}}^n\rangle e^{-i\theta^n(t)} = -\sum_n c_{\mathbf{k}}^n(t) \frac{d|v_{\mathbf{k}}^n\rangle}{dt} e^{-i\theta^n(t)}. \quad (\text{A6})$$

By multiplying $\langle v_{\mathbf{k}}^m |$ from left, we have:

$$\frac{dc_{\mathbf{k}}^m}{dt}(t) = -\sum_n c_{\mathbf{k}}^n(t) \langle v_{\mathbf{k}}^m | \frac{d|v_{\mathbf{k}}^n\rangle}{dt} e^{i(\theta^m(t) - \theta^n(t))}, \quad (\text{A7})$$

thus the first order forward differencing in time yields:

$$\begin{aligned} c_{\mathbf{k}}^m(t + \delta t) &= c_{\mathbf{k}}^m(t) \\ &\quad - \delta t \sum_n c_{\mathbf{k}}^n(t) \langle v_{\mathbf{k}}^m | \frac{d|v_{\mathbf{k}}^n\rangle}{dt} e^{i(\theta^m(t) - \theta^n(t))} + \mathcal{O}(\delta t^2). \end{aligned} \quad (\text{A8})$$

Hence, we obtain

$$\begin{aligned} c_{\mathbf{k}+\delta\mathbf{k}}^m &= c_{\mathbf{k}}^m - \sum_n c_{\mathbf{k}}^n \delta\mathbf{k} \cdot \langle v_{\mathbf{k}}^m | \nabla_{\mathbf{k}} |v_{\mathbf{k}}^n\rangle e^{i(\theta^m(t) - \theta^n(t))} \\ &= c_{\mathbf{k}}^m + \sum_n c_{\mathbf{k}}^n \delta\mathbf{k} \cdot \langle \nabla_{\mathbf{k}} v_{\mathbf{k}}^m | v_{\mathbf{k}}^n \rangle e^{i(\theta^m(t) - \theta^n(t))} \\ &= c_{\mathbf{k}}^m + \sum_n c_{\mathbf{k}}^n \left\{ \langle v_{\mathbf{k}+\delta\mathbf{k}}^m | v_{\mathbf{k}}^n \rangle - \langle v_{\mathbf{k}}^m | v_{\mathbf{k}}^n \rangle \right\} e^{i(\theta^m(t) - \theta^n(t))} \\ &= c_{\mathbf{k}}^m + \sum_n c_{\mathbf{k}}^n \left\{ \langle v_{\mathbf{k}+\delta\mathbf{k}}^m | v_{\mathbf{k}}^n \rangle - \delta_{m,n} \right\} e^{i(\theta^m(t) - \theta^n(t))} \\ &= \sum_n c_{\mathbf{k}}^n \langle v_{\mathbf{k}+\delta\mathbf{k}}^m | v_{\mathbf{k}}^n \rangle e^{i(\theta^m(t) - \theta^n(t))} + \mathcal{O}(|\delta\mathbf{k}|^2), \end{aligned} \quad (\text{A9})$$

and hence:

$$c_{\mathbf{k}+\delta\mathbf{k}}^m = \sum_n c_{\mathbf{k}}^n \langle v_{\mathbf{k}+\delta\mathbf{k}}^m | v_{\mathbf{k}}^n \rangle e^{i(\theta^m(t) - \theta^n(t))} + \mathcal{O}(|\delta\mathbf{k}|^2). \quad (\text{A10})$$

The general solution at $t = t + \delta t$ or $\mathbf{k} = \mathbf{k} + \delta\mathbf{k}$ is therefore

$$|\Psi(t + \delta t)\rangle = \sum_m c_{\mathbf{k}+\delta\mathbf{k}}^m |v_{\mathbf{k}+\delta\mathbf{k}}^m\rangle e^{-i\theta^m(t)}. \quad (\text{A11})$$

If the initial condition is,

$$c_{\mathbf{k}}^n = \delta_{n,n_0}, \quad (\text{A12})$$

then, after removing the dynamical phase factor, we obtain

$$|u_{\mathbf{k}+\delta\mathbf{k}}^{n_0}\rangle = \left\{ \sum_m |v_{\mathbf{k}+\delta\mathbf{k}}^m\rangle \langle v_{\mathbf{k}+\delta\mathbf{k}}^m| \right\} |u_{\mathbf{k}}^{n_0}\rangle + \mathcal{O}(|\delta\mathbf{k}|^2), \quad (\text{A13})$$

which reproduces Eq. (32).

Appendix B: Equation for Berry Connection Derived from Eigenvalue Equation for Translation Operator

When WFs defined by Eq. (22) satisfy:

$$\langle \Psi_{\mathbf{k}}^m | e^{i\delta\mathbf{k}\cdot\hat{\mathbf{x}}} | W_0^s \rangle = e^{i\delta\mathbf{k}\cdot\mathbf{x}_0} \langle \Psi_{\mathbf{k}}^m | W_0^s \rangle, \mathbf{x}_0 \in [0, 1)^d \quad (\text{B1})$$

for $\mathbf{k} \in \mathbb{K}_I$:

$$\begin{aligned} L \langle \Psi_{\mathbf{k}}^m | e^{i\delta\mathbf{k}\cdot\hat{\mathbf{x}}} | W_0^s \rangle &= \sqrt{L} \langle \Psi_{\mathbf{k}}^m | \sum_{\mathbf{p}} e^{i(\mathbf{p}+\delta\mathbf{k})\cdot\hat{\mathbf{x}}} | u_{\mathbf{p}}^s \rangle \\ &= \langle v_{\mathbf{k}}^m | e^{-i\mathbf{k}\cdot\hat{\mathbf{x}}} \sum_{\mathbf{p}} e^{i\mathbf{p}\cdot\hat{\mathbf{x}}} | u_{\mathbf{p}-\delta\mathbf{k}}^s \rangle \\ &= \langle v_{\mathbf{k}}^m | u_{\mathbf{k}-\delta\mathbf{k}}^s \rangle \\ &= \langle v_{\mathbf{k}}^m | \sum_n f_{\mathbf{k}-\delta\mathbf{k}}^{s,n} | v_{\mathbf{k}-\delta\mathbf{k}}^n \rangle \\ &= \sum_n f_{\mathbf{k}-\delta\mathbf{k}}^{s,n} \langle v_{\mathbf{k}}^m | v_{\mathbf{k}-\delta\mathbf{k}}^n \rangle, \end{aligned} \quad (\text{B2})$$

and also,

$$\begin{aligned} L \langle \Psi_{\mathbf{k}}^m | e^{i\delta\mathbf{k}\cdot\hat{\mathbf{x}}} | W_0^s \rangle &= e^{i\delta\mathbf{k}\cdot\mathbf{x}_0} \langle v_{\mathbf{k}}^m | e^{-i\mathbf{k}\cdot\hat{\mathbf{x}}} \sum_{\mathbf{p}} e^{i\mathbf{p}\cdot\hat{\mathbf{x}}} | u_{\mathbf{p}}^s \rangle \\ &= e^{i\delta\mathbf{k}\cdot\mathbf{x}_0} \langle v_{\mathbf{k}}^m | u_{\mathbf{k}}^s \rangle \\ &= e^{i\delta\mathbf{k}\cdot\mathbf{x}_0} \langle v_{\mathbf{k}}^m | \sum_n f_{\mathbf{k}}^{s,n} | v_{\mathbf{k}}^n \rangle \\ &= e^{i\delta\mathbf{k}\cdot\mathbf{x}_0} f_{\mathbf{k}}^{s,m}, \end{aligned} \quad (\text{B3})$$

and hence, it leads to the following equation composed of the periodic parts:

$$f_{\mathbf{k}}^{s,m} = e^{-i\delta\mathbf{k}\cdot\mathbf{x}_0} \sum_n f_{\mathbf{k}-\delta\mathbf{k}}^{s,n} \langle v_{\mathbf{k}}^m | v_{\mathbf{k}-\delta\mathbf{k}}^n \rangle + \mathcal{O}(|\delta\mathbf{k}|^2), \quad (\text{34})$$

By multiplying $|v_{\mathbf{k}}^n\rangle$ to both sides and summing over n , the energy bands are reconstructed in the following way:

$$\begin{aligned} |u_{\mathbf{k}}^s\rangle &= \sum_m f_{\mathbf{k}}^{s,m} |v_{\mathbf{k}}^m\rangle \\ &= \sum_m \left\{ \sum_n f_{\mathbf{k}-\delta\mathbf{k}}^{s,n} \langle v_{\mathbf{k}}^m | v_{\mathbf{k}-\delta\mathbf{k}}^n \rangle \right\} |v_{\mathbf{k}}^m\rangle e^{-i\delta\mathbf{k}\cdot\mathbf{x}_0} \\ &= \left\{ \sum_m |v_{\mathbf{k}}^m\rangle \langle v_{\mathbf{k}}^m| \right\} \left\{ \sum_n |v_{\mathbf{k}-\delta\mathbf{k}}^n\rangle f_{\mathbf{k}-\delta\mathbf{k}}^{s,n} e^{-i\delta\mathbf{k}\cdot\mathbf{x}_0} \right\} \\ &= e^{-i\delta\mathbf{k}\cdot\mathbf{x}_0} \left\{ \sum_m |v_{\mathbf{k}}^m\rangle \langle v_{\mathbf{k}}^m| \right\} |u_{\mathbf{k}-\delta\mathbf{k}}^s\rangle + \mathcal{O}(|\delta\mathbf{k}|^2), \end{aligned} \quad (\text{B4})$$

which gives the following projection equation:

$$|u_{\mathbf{k}}^s\rangle = e^{-i\delta\mathbf{k}\cdot\mathbf{x}_0} \left\{ \sum_m |v_{\mathbf{k}}^m\rangle \langle v_{\mathbf{k}}^m| \right\} |u_{\mathbf{k}-\delta\mathbf{k}}^s\rangle + \mathcal{O}(|\delta\mathbf{k}|^2), \quad (\text{35})$$

which is also nearly identical to:

$$\begin{aligned} |u_{\mathbf{k}+\delta\mathbf{k}}^{n_0}\rangle &= |\Psi(t+\delta t)\rangle \\ &= \left\{ \sum_m |u_{\mathbf{k}+\delta\mathbf{k}}^m\rangle \langle u_{\mathbf{k}+\delta\mathbf{k}}^m| \right\} |u_{\mathbf{k}}^{n_0}\rangle + \mathcal{O}(\delta\mathbf{k}^2). \end{aligned} \quad (\text{32})$$

Appendix C: Supplemental Calculation Related to Kato's Formula

1. Supplemental Calculation to Kato's Formula

Since

$$\begin{aligned} -i\hat{P}(\mathbf{k}+\delta\mathbf{k})\hat{E}(\mathbf{k})\hat{P}(\mathbf{k}) &= \hat{P}(t+\delta t) \left[\dot{\hat{P}}(t), \hat{P}(t) \right] \hat{P}(t) \\ &= \hat{P}(t+\delta t) \dot{\hat{P}}(t) \hat{P}(t) \hat{P}(t) \\ &\quad - \hat{P}(t+\delta t) \hat{P}(t) \dot{\hat{P}}(t) \hat{P}(t) \\ &= \left(\hat{P}(t) + \delta t \dot{\hat{P}}(t) + \mathcal{O}(\delta t^2) \right) \dot{\hat{P}}(t) \hat{P}(t) \\ &= \delta t \dot{\hat{P}}(t) \dot{\hat{P}}(t) \hat{P}(t) + \mathcal{O}(\delta t^2) \\ &= \delta t \dot{\mathbf{k}} \nabla \hat{P}(\mathbf{k}) \dot{\mathbf{k}} \nabla \hat{P}(\mathbf{k}) \hat{P}(t) + \mathcal{O}(\delta t^2) \\ &= \mathcal{O}(\delta\mathbf{k}^2), \end{aligned} \quad (\text{C1})$$

and,

$$\hat{U}(\mathbf{k}) = I - i\delta t \hat{E}(\mathbf{k}) + \mathcal{O}(\delta\mathbf{k}^2), \quad (\text{C2})$$

the following holds,

$$\begin{aligned} \hat{P}(\mathbf{k}+\delta\mathbf{k})U(\mathbf{k})\hat{P}(\mathbf{k}) &= \hat{P}(\mathbf{k}+\delta\mathbf{k})\hat{P}(\mathbf{k}) + (\delta\mathbf{k}\nabla\hat{P}(\mathbf{k}))^2\hat{P}(\mathbf{k}) \\ &= \hat{P}(\mathbf{k}+\delta\mathbf{k})\hat{P}(\mathbf{k}) + \mathcal{O}(|\delta\mathbf{k}|^2). \end{aligned} \quad (\text{C3})$$

2. Supplemental Calculation for (51)

By definition,

$$\hat{P}(\mathbf{k}) = \hat{P}(\mathbf{k}(t)) = \hat{P}(t), \quad (\text{C4})$$

where,

$$\hat{P}(\mathbf{k}) = \sum_n |v_{\mathbf{k}}^n\rangle \langle v_{\mathbf{k}}^n|. \quad (\text{C5})$$

Since,

$$\begin{aligned} \hat{P}(t)\hat{P}(t) &= \hat{P}(t), \\ \frac{d}{dt} (\hat{P}(t)\hat{P}(t)) &= \dot{\hat{P}}(t)\hat{P}(t) + \hat{P}(t)\dot{\hat{P}}(t). \end{aligned} \quad (\text{C6})$$

the following holds,

$$\dot{\hat{P}}(\mathbf{k}) = \hat{P}(\mathbf{k})\dot{\hat{P}}(\mathbf{k}) + \dot{\hat{P}}(\mathbf{k})\hat{P}(\mathbf{k}), \quad (\text{C7})$$

where $\hat{P}(\mathbf{k}) \in C^1$ is assumed. By multiplying $\dot{\hat{P}}(\mathbf{k})$ on both sides of the above equation, we have,

$$\dot{\hat{P}}(\mathbf{k})\dot{\hat{P}}(\mathbf{k})\hat{P}(\mathbf{k}) = 0. \quad (\text{C8})$$

Thus,

$$\begin{aligned} \hat{P}(\mathbf{k} + \delta\mathbf{k}) &= \hat{P}(\mathbf{k}) + \delta t \dot{\hat{P}}(\mathbf{k}) + \mathcal{O}(\delta\mathbf{k}^2) \\ \hat{P}(\mathbf{k})\hat{P}(\mathbf{k} + \delta\mathbf{k})\hat{P}(\mathbf{k}) &= \hat{P}(\mathbf{k}) + \delta t \dot{\hat{P}}(\mathbf{k})\hat{P}(\mathbf{k})\hat{P}(\mathbf{k}) + \mathcal{O}(\delta\mathbf{k}^2) \\ &= \hat{P}(\mathbf{k}) + \mathcal{O}(\delta\mathbf{k}^2). \end{aligned} \quad (\text{C9})$$

And hence, if the following holds,

$$\langle u_{\mathbf{k}}^{n_0} | u_{\mathbf{k}}^{n_1} \rangle = \delta_{n_0, n_1}, \quad (\text{C10})$$

the equation below follows:

$$\begin{aligned} \langle u_{\mathbf{k}+\delta\mathbf{k}}^{s_0} | u_{\mathbf{k}+\delta\mathbf{k}}^{s_1} \rangle &= \langle u_{\mathbf{k}}^{s_0} | \left\{ \sum_{m_0} |v_{\mathbf{k}+\delta\mathbf{k}}^{m_0}\rangle \langle v_{\mathbf{k}+\delta\mathbf{k}}^{m_0}| \right\} \\ &\quad \left\{ \sum_{m_0, m_1} |v_{\mathbf{k}+\delta\mathbf{k}}^{m_1}\rangle \langle v_{\mathbf{k}+\delta\mathbf{k}}^{m_1}| \right\} | u_{\mathbf{k}}^{s_1} \rangle \\ &= \langle u_{\mathbf{k}}^{s_0} | \hat{P}(\mathbf{k} + \delta\mathbf{k}) | u_{\mathbf{k}}^{s_1} \rangle \\ &= \langle u_{\mathbf{k}}^{s_0} | \hat{P}(\mathbf{k}) \hat{P}(\mathbf{k} + \delta\mathbf{k}) \hat{P}(\mathbf{k}) | u_{\mathbf{k}}^{s_1} \rangle \\ &= \langle u_{\mathbf{k}}^{s_0} | \hat{P}(\mathbf{k}) | u_{\mathbf{k}}^{s_1} \rangle + \mathcal{O}(\delta\mathbf{k}^2) \\ &= \delta_{s_0, s_1} + \mathcal{O}(\delta\mathbf{k}^2). \end{aligned} \quad (\text{C11})$$

Appendix D: Sinc and Wannier Centers

1. Calculation related to sinc

In one dimension, the expansion of a WF by another set of WF becomes as follows:

$$\begin{aligned} |W_n(s)\rangle &= \sum_m |W_m(r)\rangle \langle W_m(r) | W_n(s)\rangle \\ &= \sum_m \left\{ \frac{1}{L} \sum_k e^{ik(m-n-s+r)} \right\} |W_m(r)\rangle \\ &= \sum_m \text{sinc}(m-n+r-s) |M_m(r)\rangle, \end{aligned} \quad (\text{D1})$$

When the summation over the k-space is approximated by an integral, the following is used in the present paper:

$$\begin{aligned} \lim_{\delta k \rightarrow 0} \frac{1}{L} \sum_k e^{ik(x-m)} &= \lim_{L \rightarrow \infty} \frac{1}{2\pi} \sum_n e^{i\frac{2\pi n}{L}(x-m)} \left(\frac{2\pi}{L} \right) \\ &= \frac{1}{2\pi} \int_{-\pi}^{\pi} e^{ik(x-m)} dk \\ &= \text{sinc}(x-m). \end{aligned} \quad (\text{D2})$$

The following identities are used to calculate the matrix element transformation:

$$\sum_m \text{sinc}(s+m-n) \text{sinc}(s+m) = \delta_{n,0}. \quad (\text{D3})$$

The above equation is easily checked by putting it back to the form of Eq. (D2).

By utilizing the following identity [60],

$$\sum_m \frac{1}{m+x} = \pi \cot \pi x, \quad (\text{D4})$$

the following summation rule is obtained:

$$\begin{aligned} \sum_m (m+x) \text{sinc}^2(m+x) &= \sum (m+x) \frac{\sin^2 \pi x}{\pi^2 (m+x)^2} \\ &= \frac{\sin^2 \pi x}{\pi^2} \sum \frac{1}{m+x} \\ &= \frac{\sin^2 \pi x}{\pi^2} \pi \cot \pi x \\ &= \frac{1}{2\pi} \sin 2\pi x, \end{aligned} \quad (\text{D5})$$

2. Convergence of r^n to x_0

The convergence of the iteration is examined by introducing the following function:

$$F(r) = r + \frac{1}{2\pi} \sin(2\pi(x_0 - r)) \pmod{1}. \quad (\text{D6})$$

Since

$$\left| \frac{dF(r)}{dr} \right| = 1 - \cos(2\pi(x_0 - r)) < 1, \quad (0 < x_0 - r < 1/4), \quad (\text{D7})$$

x_0 is an attractor [61]. Therefore, letting,

$$e_n = 2\pi(x_0 - r^n) \in (-\pi, \pi], \quad (\text{D8})$$

we have,

$$e_{n+1} = e_n - \sin e_n, \quad |e_{n+1}| \leq |e_n| \text{ for } |e_n| < \pi, \quad (\text{D9})$$

Since

$$|e_n| < \pi, \quad (\text{D10})$$

we find,

$$|e_{n+1}| < |e_n|, \quad (\text{D11})$$

with equality only at $e_n = \pm\pi$. This means the error becomes always smaller in any step of the iteration. Therefore,

$$\lim_{n \rightarrow \infty} r^n = x_0. \quad (\text{D12})$$

The order of convergence is cubic. When $e_n \ll 1$, from Eq. (D9),

$$\begin{aligned} e_{n+1} &= e_n - \left(e_n - \frac{1}{6}e_n^3\right) \\ &= \frac{1}{6}e_n^3 \end{aligned} \quad (\text{D12})$$

and hence,

$$\lim_{e_n \rightarrow 0} \frac{|e_{n+1}|}{|e_n|^3} = \frac{1}{6}. \quad (\text{D13})$$

3. Direct Derivation of Sinc-Loop

Since the initial *corrugated* Berry connection is swept flat, the swell developed over the border carries all the information. By segregating the *cross-border* term out of the summation, the matrix element of $e^{i\delta k \hat{x}}$ is estimated by solving the following simplified equations:

$$\begin{aligned} L\langle W_0(r)|e^{i\delta k \hat{x}}|W_0(r)\rangle &= \sum_{k=-\pi+\delta k}^{\pi-\delta k} \langle u_k|u_{k-\delta k}\rangle e^{i\delta k r} \\ &+ \langle u_{-\pi}^0|e^{2i\pi \hat{x}}|u_{\pi-\delta k}^0\rangle e^{-2i\pi r}. \end{aligned} \quad (\text{D14})$$

And we assume the phases of $\{|u_k\rangle\}$ are aligned and,

$$\langle u_k|u_{k-\delta k}\rangle = 1, (k \in \mathbb{K}_I), \quad (\text{D15})$$

and,

$$L\langle W_0(r)|e^{i\delta k \hat{x}}|W_0(r)\rangle = \begin{cases} L(1 + \alpha(r))e^{i\delta k X_{0,0}(r)} & (r \neq x_0) \\ L(1 + \alpha(x_0))e^{i\delta k x_0} & (r = x_0) \end{cases}, \quad (\text{D16})$$

where $\alpha(r)$ is a factor expressing the deviation of $e^{i\delta k \hat{x}}$ from being unitary.

$$\alpha(r) = \left| \langle W_0(r)|e^{i\delta k \hat{x}}|W_0(r)\rangle \right| - 1 \sim \mathcal{O}(\delta k), \quad (\text{D17})$$

and by definition,

$$\alpha(x_0) = 0. \quad (\text{D18})$$

Except for the cross-border term, the right-hand-side of Eq. (D14) is basically proportional to $e^{i\delta k r}$ regardless of the value of r . Thus, the task is to find x_0 which least disturbs the proportionality. By simultaneously solving Eqs. (D14) and (D16) for $r = x_0$ and $r \neq x_0$, we have:

$$\begin{aligned} L(1 + \alpha(r))e^{i\delta k X_{0,0}(r)} &= (L-1)e^{i\delta k r} + \langle u_{-\pi}^0|e^{2i\pi \hat{x}}|u_{\pi-\delta k}^0\rangle e^{-2i\pi r} \\ L(1 + \alpha(x_0))e^{i\delta k x_0} &= (L-1)e^{i\delta k x_0} + \langle u_{-\pi}^0|e^{2i\pi \hat{x}}|u_{\pi-\delta k}^0\rangle e^{-2i\pi x_0}. \end{aligned} \quad (\text{D19})$$

By using $\delta k L = 2\pi$, we have,

$$1 + \alpha(r)L + i(1 + \alpha(r))2\pi X_{0,0}(r) - 2\pi i r = e^{2i\pi x_0} + \mathcal{O}(\delta k). \quad (\text{D20})$$

And hence,

$$\begin{aligned} (1 + \alpha(x_0))2\pi(X_{0,0}(r) - r) &= \sin 2\pi(x_0 - r) \\ 1 + \alpha(r)L &= \cos 2\pi(x_0 - r). \end{aligned} \quad (\text{D21})$$

The first line of Eq. (D21) is a reproduction of Eq. (73) with the deviation factor $\alpha(r) \sim \mathcal{O}(\delta k)$. And the second line shows the relationship between $\alpha(r)$ and r . The verification of Eq. (D21) is shown in Fig. 25.

4. Supplemental Calculation for Eq. (73)

For,

$$X_{M_1, M_2}(x_0) = \delta_{M_{1,x}, M_{2,x}} \delta_{M_{1,y}, M_{2,y}} \delta_{M_{1,z}, M_{2,z}} (M_{1,x} + x_0), \quad (\text{D22})$$

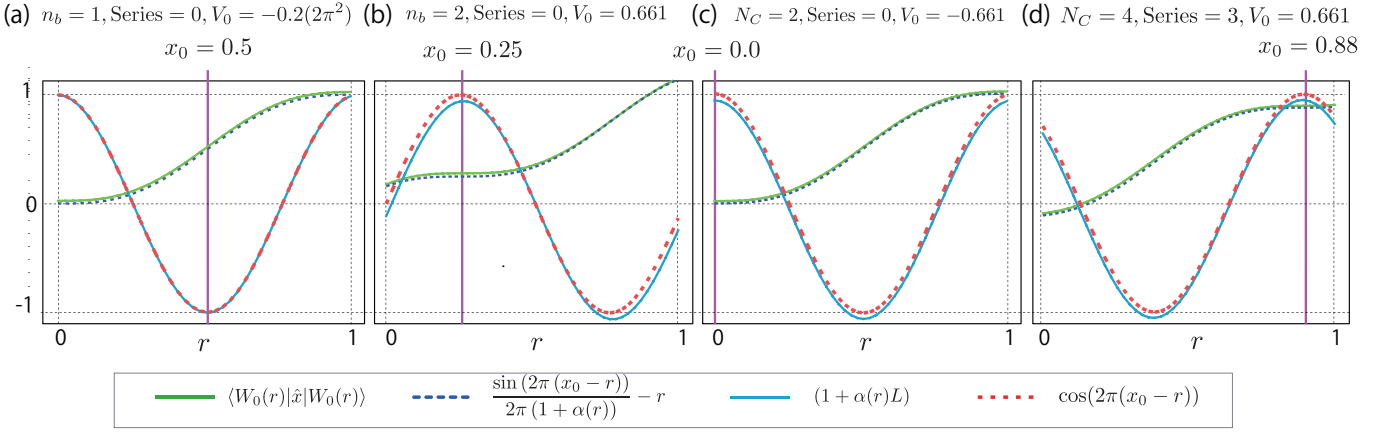


FIG. 25. (Color online) Verification of Eq. (D20) in single- and composite-band cases. N_C denotes the number of the energy bands composing the composite band systems. n_b indicates the energy band index of the single-band system. The series numbers for composite-band cases are labeled #0, #1, #2, #3 from the left side of a unit cell. Panels (a) to (d) correspond to Figs. 5(a), 5(b), 8(a) and 8(b). The MLWFs are found in Figs. 6 and 9.

$X_{00}(\mathbf{r})$ is calculated as follows:

$$\begin{aligned}
 X_{00}(\mathbf{r}) &= \langle W_0(\mathbf{r}) | \hat{x} | W_0(\mathbf{r}) \rangle \\
 &= \left\{ \sum_{N_{1,x}, N_{2,x}} \text{sinc}(N_{1,x} + r_x - x_0) \text{sinc}(N_{2,x} + r_x - x_0) \delta_{N_{1,x}, N_{2,x}} (N_{1,x} + x_0) \right\} \\
 &\quad \left\{ \sum_{N_{1,y}, N_{2,y}} \text{sinc}(N_{1,y} + r_y) \text{sinc}(N_{2,y} + r_y) \delta_{N_{1,y}, N_{2,y}} \right\} \left\{ \sum_{N_{1,z}, N_{2,z}} \text{sinc}(N_{1,z} + r_z) \text{sinc}(N_{2,z} + r_z) \delta_{N_{1,z}, N_{2,z}} \right\} \quad (\text{D23}) \\
 &= \left\{ \sum_{N_{1,x}} \text{sinc}^2(N_{1,x} + r_x - x_0) (N_{1,x} + x_0) \right\} \left\{ \sum_{N_{1,y}} \text{sinc}^2(N_{1,y} + r_y) \right\} \left\{ \sum_{N_{1,z}} \text{sinc}^2(N_{1,z} + r_z) \right\} \\
 &= \left\{ \frac{\sin 2\pi(x_0 - r_x)}{2\pi} + r_x \right\}.
 \end{aligned}$$

Appendix E: Calculation Setting for Graphene

A hexagonal cell (`ibrav` = 4) with $a = 4.602$ bohr (2.435 Å) and $c = 18.408$ bohr (9.74 Å) was used, containing two carbon atoms at fractional coordinates (0, 0, 0) and (1/3, 2/3, 0). Plane-wave cutoffs of `ecutwfc` = 100 Ry and `ecutrho` = 500 Ry were adopted. Brillouin-zone sampling employed an $N \times N \times 1$ mesh (e.g., $26 \times 26 \times 1$), and Methfessel–Paxton smearing with `degauss` = 0.01 Ry was used. For the Wannier analysis we used W90 with `num_bands` = 5 and `num_wann` = 5 on the same k -mesh (e.g., `mp_grid` = 26 26 1), starting from initial projections consisting of $C-p_z$ orbitals and three bond-centered s -like orbitals.

Appendix F: Reciprocal-space formulas and seam diagnostics for graphene

This appendix reformulates the standard reciprocal-space spread expressions [10, 13, 14] to provide a rigorous theoret-

ical basis for the $\mathcal{O}(L)$ scaling observed in Sec. VIC. The purpose is to explicitly evaluate the geometric gauge defects using two complementary diagnostics, the single-state overlap σ_α^s and the subspace-level overlap σ_{\min} .

1. Nearest-neighbor overlaps and discrete measure

For each nearest-neighbor link $\delta \mathbf{k}_\alpha$ ($\alpha \in \mathcal{N}$), we define the overlap matrix

$$M_{sp}^\alpha(\mathbf{k}) = \langle u_{\mathbf{k}}^s | u_{\mathbf{k} + \delta \mathbf{k}_\alpha}^p \rangle. \quad (\text{F1})$$

We also introduce the discrete measure

$$v_\alpha = \frac{w_\alpha}{N_{\mathbf{k}}}, \quad N_{\mathbf{k}} = L^2, \quad (\text{F2})$$

so that the weights do not appear explicitly in the local kernels discussed below. On a uniform mesh, $v_\alpha = \mathcal{O}(L^0)$. Using

Eq. (F2), the Marzari–Vanderbilt decomposition becomes

$$\Omega = \Omega_I + \Omega_{OD} + \Omega_D, \quad (\text{F3})$$

with

$$\Omega_I = \sum_{\mathbf{k}, \alpha} v_\alpha \left(J - \sum_{s,p} |M_{sp}^\alpha(\mathbf{k})|^2 \right), \quad (\text{F4})$$

$$\Omega_{OD} = \sum_{\mathbf{k}, \alpha} v_\alpha \sum_{s \neq p} |M_{sp}^\alpha(\mathbf{k})|^2, \quad (\text{F5})$$

$$\Omega_D = \sum_{\mathbf{k}, \alpha} v_\alpha \sum_s [\Im \log M_{ss}^\alpha(\mathbf{k}) + \delta \mathbf{k}_\alpha \cdot \mathbf{x}_0^s]^2. \quad (\text{F6})$$

The seam analysis below uses only the amplitude part of the links. The phase contribution in Ω_D belongs to the full spread functional, but it is not needed for the curvature diagnostics introduced here.

2. Single-band(series) distortion carried by an extracted MLWF

For a fixed extracted series s , we consider the diagonal link

$$m_\alpha^s(\mathbf{k}) = M_{ss}^\alpha(\mathbf{k}) = \langle u_{\mathbf{k}}^s | u_{\mathbf{k}+\delta \mathbf{k}_\alpha}^s \rangle. \quad (\text{F7})$$

Because this is a 1×1 overlap matrix, its singular value is simply

$$\sigma_\alpha^s(\mathbf{k}) = |m_\alpha^s(\mathbf{k})|. \quad (\text{F8})$$

We then define the corresponding single-state kernel by

$$\omega_\alpha^s(\mathbf{k}) = 1 - [\sigma_\alpha^s(\mathbf{k})]^2 = 1 - |m_\alpha^s(\mathbf{k})|^2. \quad (\text{F9})$$

Equation (F9) is the explicit relation between σ_α^s and ω_α^s . Thus ω_α^s measures how far the one-dimensional subspace carried by the s -th Wannier series departs from perfect continuity across the link $\delta \mathbf{k}_\alpha$. No logarithmic phase term is included here, because the present diagnostic is meant to isolate the curvature of the carried one-dimensional subspace itself.

3. Subspace-level diagnostic for the residual transported space

The complementary diagnostic for the transported J -dimensional subspace is the minimum singular value of the full overlap matrix:

$$\sigma_{\min}(\mathbf{k}; \delta \mathbf{k}_\alpha) = \min_i \sigma_i(M^\alpha(\mathbf{k})) = \cos \theta_{\max}. \quad (\text{F10})$$

The associated defect is

$$d_\alpha(\mathbf{k}) = 1 - \sigma_{\min}^2(\mathbf{k}; \delta \mathbf{k}_\alpha). \quad (\text{F11})$$

Equation (F10) measures the mismatch of the neighboring J -dimensional transported subspaces, whereas Eq. (F9) measures the geometric curvature of the one-dimensional subspace carried by a particular extracted MLWF. Both quantities are evaluated strictly in reciprocal space using the unified discrete measure v_α .

4. Order evaluation of the boundary seam defects

Appendix D 3 shows that the interior links along each transported string are flattened, so the nontrivial geometric mismatch is pushed entirely to the boundary seam. Let β denote the link direction in which the seam appears after the first extraction. The order evaluations of the single-state and subspace-level diagnostics on this boundary are strictly $\mathcal{O}(L^0)$:

$$\begin{cases} \omega_\beta^1(\mathbf{k}) = \mathcal{O}(L^0) \\ d_\beta(\mathbf{k}) = 1 - \sigma_{\min}^2(\mathbf{k}; \delta \mathbf{k}_\beta) = \mathcal{O}(L^0) \end{cases} \quad (\mathbf{k} \in \text{seam}). \quad (\text{F12})$$

Equivalently, the singular values themselves exhibit a constant $\mathcal{O}(L^0)$ floor:

$$\begin{cases} \sigma_\beta^1(\mathbf{k}) = \mathcal{O}(L^0) \\ \sigma_{\min}(\mathbf{k}; \delta \mathbf{k}_\beta) = \mathcal{O}(L^0) \end{cases} \quad (\mathbf{k} \in \text{seam}). \quad (\text{F13})$$

These finite $\mathcal{O}(L^0)$ evaluations confirm that neither the single-state nor the subspace-level local kernels develop any anomalous L -dependent divergence. The macroscopic accumulation of these local defects over the seam, which yields the $\mathcal{O}(L)$ scaling of the total spread, is explicitly evaluated in Sec. VIC.

[1] G. H. Wannier, The structure of electronic excitation levels in insulating crystals, *Phys. Rev.* **52**, 191 (1937).
[2] I. Adams, E. N., The Crystal Momentum as a Quantum Mechanical Operator, *The Journal of Chemical Physics* **21**, 2013 (1953).
[3] E. N. Adams, Motion of an electron in a perturbed periodic potential, *Phys. Rev.* **85**, 41 (1952).
[4] E. I. Blount, Bloch electrons in a magnetic field, *Phys. Rev.* **126**, 1636 (1962).

[5] S. Kivelson, Wannier functions in one-dimensional disordered systems: Application to fractionally charged solitons, *Phys. Rev. B* **26**, 4269 (1982).
[6] W. Kohn, Analytic properties of Bloch waves and Wannier functions, *Phys. Rev.* **115**, 809 (1959).
[7] J. D. Cloizeaux, Energy bands and projection operators in a crystal: Analytic and asymptotic properties, *Phys. Rev.* **135**, A685 (1964).
[8] W. Kohn and J. R. Onffroy, Wannier functions in a simple non-periodic system, *Phys. Rev. B* **8**, 2485 (1973).

- [9] A. Nenciu and G. Nenciu, Existence of exponentially localized wannier functions for nonperiodic systems, *Phys. Rev. B* **47**, 10112 (1993).
- [10] N. Marzari and D. Vanderbilt, Maximally localized wannier functions for composite energy bands, *Phys. Rev. B* **56**, 12847 (1997).
- [11] I. Souza, N. Marzari, and D. Vanderbilt, Maximally localized wannier functions for entangled energy bands, *Phys. Rev. B* **65**, 035109 (2001).
- [12] N. Marzari, A. A. Mostofi, J. R. Yates, I. Souza, and D. Vanderbilt, Maximally localized wannier functions: Theory and applications, *Rev. Mod. Phys.* **84**, 1419 (2012).
- [13] A. A. Mostofi, J. R. Yates, Y.-S. Lee, I. Souza, D. Vanderbilt, and N. Marzari, wannier90: A tool for obtaining maximally-localised wannier functions, *Computer Physics Communications* **178**, 685 (2008).
- [14] G. Pizzi, V. Vitale, R. Arita, S. Blügel, F. Freimuth, G. Géranton, M. Gibertini, D. Gresch, C. Johnson, T. Koretsune, J. Ibañez-Azpiroz, H. Lee, J.-M. Lihm, D. Marchand, A. Marrazzo, Y. Mokrousov, J. I. Mustafa, Y. Nohara, Y. Nomura, L. Paulatto, S. Poncé, T. Ponweiser, J. Qiao, F. Thöle, S. S. Tsirkin, M. Wierzbowska, N. Marzari, D. Vanderbilt, I. Souza, A. A. Mostofi, and J. R. Yates, Wannier90 as a community code: new features and applications, *Journal of Physics: Condensed Matter* **32**, 165902 (2020).
- [15] D. Vanderbilt and R. D. King-Smith, Electric polarization as a bulk quantity and its relation to surface charge, *Physical Review B* **48**, 4442 (1993).
- [16] R. Resta, Macroscopic polarization in crystalline dielectrics: the geometric phase approach, *Rev. Mod. Phys.* **66**, 899 (1994).
- [17] X. Wu, O. Diéguez, K. M. Rabe, and D. Vanderbilt, Wannier-based definition of layer polarizations in perovskite superlattices, *Phys. Rev. Lett.* **97**, 107602 (2006).
- [18] M. G. Lopez, D. Vanderbilt, T. Thonhauser, and I. Souza, Wannier-based calculation of the orbital magnetization in crystals, *Phys. Rev. B* **85**, 014435 (2012).
- [19] J. D. Cloizeaux, Orthogonal orbitals and generalized wannier functions, *Phys. Rev.* **129**, 554 (1963).
- [20] V. P. Smirnov and D. E. Usvyat, Variational method for the generation of localized wannier functions on the basis of bloch functions, *Phys. Rev. B* **64**, 245108 (2001).
- [21] K. Busch, S. F. Mingaleev, A. Garcia-Martin, M. Schillinger, and D. Hermann, The wannier function approach to photonic crystal circuits, *Journal of Physics: Condensed Matter* **15**, R1233 (2003).
- [22] K. Busch, C. Blum, A. M. Graham, D. Hermann, M. Köhl, P. Mack, and C. Wolff, The photonic wannier function approach to photonic crystal simulations: status and perspectives, *Journal of Modern Optics* **58**, 365 (2011).
- [23] C. Wolff, P. Mack, and K. Busch, Generation of wannier functions for photonic crystals, *Phys. Rev. B* **88**, 075201 (2013).
- [24] Y. Liu, W. Cao, W. Chen, H. Wang, L. Yang, and X. Zhang, Fully integrated topological electronics, *Scientific Reports* **12**, 13410 (2022).
- [25] V. H. Pham, H. Bui, T. V. Nguyen, T. A. Nguyen, T. S. Pham, V. D. Pham, T. C. Tran, T. T. Hoang, and Q. M. Ngo, Progress in the research and development of photonic structure devices, *Advances in Natural Sciences: Nanoscience and Nanotechnology* **7**, 015003 (2016).
- [26] H. Takeda, A. Chutinan, and S. John, Localized light orbitals: Basis states for three-dimensional photonic crystal microscale circuits, *Phys. Rev. B* **74**, 195116 (2006).
- [27] B. Simon, Holonomy, the quantum adiabatic theorem, and berry's phase, *Physical Review Letters* **51**, 2167 (1983).
- [28] M. V. Berry, Quantal phase factors accompanying adiabatic changes, *Proceedings of the Royal Society of London. Series A, Mathematical and Physical Sciences* **392**, 45 (1984).
- [29] R. Yu, X.-L. Qi, B. A. Bernevig, Z. Fang, and X. Dai, Equivalent expression of \mathbb{Z}_2 topological invariant using non-abelian berry connection, *Phys. Rev. B* **84**, 075119 (2011).
- [30] A. A. Soluyanov and D. Vanderbilt, Computing topological invariants without inversion symmetry, *Phys. Rev. B* **83**, 235401 (2011).
- [31] A. Alexandradinata, X. Dai, and B. A. Bernevig, Wilson-loop characterization of inversion-symmetric topological insulators, *Phys. Rev. B* **89**, 155114 (2014).
- [32] C. Brouder, G. Panati, M. Calandra, C. Mourougane, and N. Marzari, Exponential localization of wannier functions in insulators, *Phys. Rev. Lett.* **98**, 046402 (2007).
- [33] J. I. Mustafa, S. Coh, M. L. Cohen, and S. G. Louie, Automated construction of maximally localized wannier functions: Optimized projection functions method, *Phys. Rev. B* **92**, 165134 (2015).
- [34] A. Damle, L. Lin, and L. Ying, Compressed representation of kohn–sham orbitals via selected columns of the density matrix, *Journal of Chemical Theory and Computation* **11**, 1463 (2015), pMID: 26574357.
- [35] A. Damle, L. Lin, and L. Ying, Scdm-k: Localized orbitals for solids via selected columns of the density matrix (2016), arXiv:1507.03354 [physics.comp-ph].
- [36] K. D. Stubbs, A. B. Watson, and J. Lu, Iterated projected position algorithm for constructing exponentially localized generalized wannier functions for periodic and nonperiodic insulators in two dimensions and higher, *Phys. Rev. B* **103**, 075125 (2021).
- [37] T. Kato, On the adiabatic theorem of quantum mechanics, *Journal of the Physical Society of Japan* **5**, 435 (1950).
- [38] J. E. Avron and A. Elgart, An adiabatic theorem without a gap condition, in *Mathematical Physics, X. International Congress on Mathematical Physics (ICMP '97)*, Progress in Mathematical Physics (Birkhäuser, 1998) pp. 1–34.
- [39] J. E. Avron and A. Elgart, Adiabatic theorem without a gap condition, *Communications in Mathematical Physics* **203**, 445 (1999).
- [40] S. Teufel, *Adiabatic Perturbation Theory in Quantum Dynamics*, Lecture Notes in Mathematics, Vol. 1821 (Springer, Berlin, Heidelberg, 2003).
- [41] J. K. Asbóth, L. Oroszlány, and A. Pályi, *A Short Course on Topological Insulators: Band-structure topology and edge states in one and two dimensions*, Lecture Notes in Physics, Vol. 919 (Springer, Cham, 2016).
- [42] J. Cayssol and J.-N. Fuchs, Topological and geometrical aspects of band theory, *Journal of Physics: Materials* **4**, 034007 (2021).
- [43] D. Vanderbilt, *Berry Phases in Electronic Structure Theory: Electric Polarization, Orbital Magnetization and Topological Insulators* (Cambridge University Press, Cambridge, 2018).
- [44] M. Galassi, J. Davies, J. Theiler, B. Gough, G. Jungman, M. Booth, and F. Rossi, *GNU Scientific Library Reference Manual*, 3rd ed. (Network Theory Ltd., Bristol, 2009).
- [45] E. Engel and R. M. Dreizler, *Density Functional Theory: An Advanced Course*, Theoretical and Mathematical Physics (Springer, 2011) appendix A: Functionals and the Functional Derivative.
- [46] I. M. Gelfand and S. V. Fomin, *Calculus of Variations* (Prentice-Hall; Dover reprint, 1963).
- [47] P. J. Olver, *The calculus of variations*, Lecture notes, Univ. of Minnesota (2022).

- [48] Functional derivative, Encyclopedia of Mathematics (EMS) (2020).
- [49] Y. Hamai and K. Wakabayashi, Approximating maximally localized wannier functions with position scaling eigenfunctions, *Phys. Rev. B* **108**, 245413 (2023).
- [50] I. Daubechies, Ten lectures on wavelets (Society for Industrial and Applied Mathematics, 1992) Chap. 6.
- [51] I. Daubechies, Orthonormal bases of compactly supported wavelets, in *Fundamental Papers in Wavelet Theory* (Princeton University Press, Princeton, 2006) pp. 564–652.
- [52] A. Vellasco-Gomes, R. de Figueiredo Camargo, and A. Bruno-Alfonso, Energy bands and wannier functions of the fractional kronig-penney model, *Applied Mathematics and Computation* **380**, 125266 (2020).
- [53] R. Wang, E. A. Lazar, H. Park, A. J. Millis, and C. A. Marianetti, Selectively localized wannier functions, *Phys. Rev. B* **90**, 165125 (2014).
- [54] J. Ahn and B.-J. Yang, Unconventional topological phase transition in two-dimensional systems with space-time inversion symmetry, *Physical Review Letters* **118**, 156401 (2017).
- [55] C. Fang and L. Fu, New classes of three-dimensional topological crystalline insulators: Nonsymmorphic and magnetic, *Physical Review B* **91**, 161105 (2015).
- [56] P. Giannozzi, S. Baroni, N. Bonini, M. Calandra, R. Car, C. Cavazzoni, D. Ceresoli, G. L. Chiarotti, M. Cococcioni, I. Dabo, A. Dal Corso, S. de Gironcoli, S. Fabris, G. Fratesi, R. Gebauer, U. Gerstmann, C. Gougoussis, A. Kokalj, M. Lazzeri, L. Martin-Samos, N. Marzari, F. Mauri, R. Mazzeo, S. Paolini, A. Pasquarello, L. Paulatto, C. Sbraccia, S. Scandolo, G. Sclauzero, A. P. Seitsonen, A. Smogunov, P. Umari, and R. M. Wentzcovitch, Quantum espresso: a modular and open-source software project for quantum simulations of materials, *Journal of Physics: Condensed Matter* **21**, 395502 (2009).
- [57] P. Giannozzi, O. Andreussi, T. Brumme, O. Bunau, M. Buongiorno Nardelli, M. Calandra, R. Car, C. Cavazzoni, D. Ceresoli, M. Cococcioni, N. Colonna, I. Carnimeo, A. Dal Corso, S. de Gironcoli, P. Delugas, R. A. DiStasio Jr., A. Ferretti, A. Floris, G. Fratesi, G. Fugallo, R. Gebauer, U. Gerstmann, F. Giustino, T. Gorni, J. Jia, M. Kawamura, H.-Y. Ko, A. Kokalj, E. Küçükbenli, M. Lazzeri, M. Marsili, N. Marzari, F. Mauri, N. L. Nguyen, H.-V. Nguyen, A. Otero-de-la Roza, L. Paulatto, S. Poncé, D. Rocca, R. Sabatini, V. Santmacri, M. Schlipf, A. P. Seitsonen, A. Smogunov, I. Timrov, T. Thonhauser, P. Umari, N. Vast, X. Wu, and S. Baroni, *Journal of Physics: Condensed Matter* **29**, 465901 (2017).
- [58] The Quantum ESPRESSO Foundation, Quantum ESPRO project website, <https://www.quantum-espresso.org/> (2026), accessed: 2026-02-07.
- [59] The Wannier90 Developers, *Wannier90 User Guide* (2026), version 3.1, Available at <http://www.wannier.org/support/>.
- [60] M. Aigner and G. M. Ziegler, *Proofs from THE BOOK*, 6th ed. (Springer Publishing Company, Incorporated, 2018).
- [61] R. L. Devaney, *An Introduction to Chaotic Dynamical Systems*, 2nd ed. (CRC Press, Boca Raton, 2003) Chap. 1.